Kinematic inversion of aseismic fault slip during the nucleation of laboratory earthquakes

P. Dublanchet[1], F.X. Passelègue [2], H. Chauris[1], A. Gesret[1], C. Twardzik[2], C. Nöel [2]

[1]Mines Paris, PSL University, Centre for geosciences, 77300 Fontainebleau, France
[2]Université Côte d'Azur, CNRS, Observatoire de la Côte d'Azur, IRD, Géoazur, Sophia Antipolis, France.

Key Points:

- We design a new kinematic slip inversion method for laboratory faults based on finite elements analysis and strain measurements
- The resolution of the method and uncertainties on inferred slip are evaluated through synthetic tests and a Bayesian framework
- Studying the nucleation of laboratory earthquakes with saw-cut samples reveals an aseismic slip event propagating at about 200 meters per day

Corresponding author: Pierre Dublanchet, `pierre.dublanchet@minesparis.psl.eu`

Abstract

Decades of geophysical monitoring have revealed the importance of slow aseismic fault slip in the release of tectonic energy. Although significant progress have been made in imaging aseismic slip on natural faults, many questions remain concerning its physical control. Here we present an attempt to study the evolution of aseismic slip in the controlled environment of the laboratory. We develop a kinematic inversion method, to image slip during the nucleation phase of a dynamic rupture within a saw-cut sample loaded in a tri-axial cell. We use the measurements from a strain gauge array placed in the vicinity of the fault, and the observed shortening of the sample, to invert the fault slip distribution in space and time. The inversion approach relies both on a deterministic optimization step followed by a Bayesian analysis. The Bayesian inversion is initiated with the best model reached by the deterministic step, and allows to quantify the uncertainties on the inferred slip history. We show that the nucleation consists of quasi-static aseismic slip event expanding along the fault at a speed of the order of 200 m.day^{-1}, before degenerating into a dynamic rupture. The total amount of aseismic slip accumulated during this nucleation phase reaches 7±2 μm locally, about 8 to 15 % of the coseismic slip. The resolution of the method is evaluated, indicating that the main limitation is related to the impossibility of measuring strain inside the rock sample. The results obtained however show that the method could improve our understanding of earthquake nucleation.

Plain Language Summary

Major faults situated at tectonic plate boundaries accommodate relative plate motion by a series of earthquakes, where an offset is created in a few seconds to minutes, or by aseismic slip episodes accumulating the same amount of slip over hours to several days. Aseismic slip events are of particular interest since they are suspected to play a role in the preparatory phase of damaging earthquakes. Measurements of ground deformation reveal how these events develop on real faults, but the physical control on this process remains elusive. Here we present an attempt to image the development of aseismic slip events in the controlled context of a laboratory experiment where a centimetric scale fault is activated by slow loading, using local deformation measurements. Our study reveals that a laboratory earthquake was preceded by an aseismic slip event expanding along the fault at a speed of the order of 200 m.day^{-1}, and accumulating locally 5 to 9 μm of relative displacement. We also discuss extensively the resolution of our method, and provide recommendations to optimize the measurements. Our method has the potential to improve significantly the interpretability of rock mechanics experiments.

1 Introduction

A significant fraction of the elastic energy stored in the upper earth crust is released in fault zones through sequences of aseismic slip events, spanning a wide range of spatial and temporal scales (Bürgmann, 2018). Many natural and induced earthquake swarms are likely to be driven by such aseismic slip events (Lohman & McGuire, 2007; Sirorattanakul et al., 2022; De Barros et al., 2020). Aseismic slip is also frequently observed during the preparatory phase of major earthquakes, or during the following postseismic period (Hsu et al., 2006; Ozawa et al., 2012). However, many aspects of the physical control on aseismic slip evolution are still poorly known, in particular regarding the expansion and acceleration of a particular event, that can either degenerate into a dynamic rupture, or stabilize. Understanding the mechanical control on aseismic slip evolution prior the nucleation and the propagation of instability is thus crucial to estimate the seismic potential of active fault zones (Avouac, 2015).

A first approach to unravel the physics of aseismic fault deformation consists of estimating the spatial and temporal evolution of slip along natural faults. However, because fault slip occurs at depth under extreme environmental conditions, direct in-situ measurements remain nowadays impossible, and these estimates are solely based on inverse problem theory (Tarantola, 2005; Ide, 2007). Such kinematic slip inversions involve dense geodetic measurements performed at the earth surface (GNSS, InSAR interferometry, creepmeters, tiltmeters) (Bürgmann, 2018). The displacements of the earth surface (attributed to fault activation) are inverted to determine slip history on faults, assuming that the bulk crust behaves as an elastic, or a visco-elastic material. When focusing on aseismic slip episodes, the inversions are generally performed in a quasi-static framework since no significant wave radiation occurs. Fully dynamic elasticity could also be accounted for to image the co-seismic earthquake ruptures (Olson & Apsel, 1982; S. H. Hartzell & Heaton, 1983; Vallée & Bouchon, 2004; Liu et al., 2006; S. Hartzell et al., 2007; Mai et al., 2016; Caballero et al., 2023; Vallée et al., 2023). Kinematic slip inversion has allowed to reveal in details the dynamics of aseismic slip in various contexts: slow slip events (SSE) in subduction zones (McGuire & Segall, 2003; Radiguet et al., 2011; Nishimura et al., 2013; Wallace et al., 2016), continuous or bursts of aseismic slip along strike slip faults (Schmidt et al., 2005; Jolivet et al., 2015), normal faults (Anderlini et al., 2016), or reverse faults (Thomas et al., 2014), afterslip (Hsu et al., 2006) and precursory slip (Ozawa et al., 2012; Twardzik et al., 2022; Boudin et al., 2022) associated with megathrust earthquakes. The resolution that could be achieved is generally limited by the resolution and the density of the data inverted, as well as the complexity of the forward problem (geometry, medium heterogeneity). In any case, translating the slip history in terms of mechanical properties of fault zones would require additional knowledge on structure, frictional properties, stress state at depth, features that are generally poorly constrained.

Alternatively, the mechanics of fault slip could also be studied in the controlled environment of the laboratory, where loading conditions and material properties can be measured. However, despite major advances in imaging fault slip on natural faults, attempts to apply the inverse methods to experimental data sets remain limited. Technical advances in experimental rock mechanics make it possible to reproduce the various stages of the seismic cycle in a high-pressure environment while monitoring the evolution of strain in the bulk of the sample. Strain gauges are commonly used to evaluate the sample mechanical response during rock deformation experiments, the elastic properties of the rock sample and the deviations from elasticity in the final stage of the experiment to macroscopic failure (Lockner et al., 1992). In addition, such strain gauges can also be used to track the change in strain during the development of the slip front (Passelègue et al., 2019, 2020) as well as during the propagation of the dynamic fracture (Passelègue et al., 2016). Here we argue that these measurements, performed under known conditions and near the fault plane, could also be used to invert the spatial and temporal evolution of slip during different stages of laboratory experiments, and in particular during the nucleation phase of stick-slip events.

Several experimental studies have attempted to characterize the evolution of slip, moment release and the dynamics of precursory acoustic emissions during this early preparatory phase (Latour et al., 2013; McLaskey & Lockner, 2014; Passelègue et al., 2017; Mclaskey & Yamashita, 2017; Selvadurai et al., 2017; McLaskey, 2019; Acosta et al., 2019; Dresen et al., 2020; Marty et al., 2023; Guérin-Marthe et al., 2023). In some of these studies, the evolution of fault slip is either derived from local slip measurements (McLaskey & Kilgore, 2013; Selvadurai et al., 2017), or from photo-elasticity (Nielsen et al., 2010; Latour et al., 2013; Guérin-Marthe et al., 2019; Gvirtzman & Fineberg, 2021, 2023), in a 2D setup. Photo-elasticity requires the use of polycarbonate or poly-methyl-methacrylate (PMMA), considered as a rock material analog. These experiments performed at low normal stress (less than 20 MPa), and metric samples, show an early quasi-static nucleation phase (Latour et al., 2013), where an aseismic slip event initiates on a critical region of the interface, and expands along the fault at speeds ranging from 0.1 $mm.s^{-1}$ to 10 $m.s^{-1}$. During this process, slip rate reaches a few $mm.s^{-1}$. Once the slip event has grown to a critical nucleation size, it degenerates into a dynamic rupture (the stick-slip event) (Gvirtzman

& Fineberg, 2021). Additionally, several studies report a stressing rate dependence of this aseismic nucleation process, where the duration of the nucleation phase and critical nucleation length decrease with increasing stressing rate (Guérin-Marthe et al., 2019, 2023), while aseismic slip fronts migrate faster (Kaneko et al., 2016).

Alternatively, a tri-axial setup allows higher confining conditions (more than 100 MPa) and slip on a 2D elliptical fault (3D setup). Photo-elasticity or direct slip measurements cannot be used in this case, but the nucleation can be tracked by strain sensors, and by acoustic monitoring systems. This latter approach aims at capturing the migration, rate and magnitudes of acoustic emissions, considered as a by-product of aseismic slip acceleration (McLaskey & Lockner, 2014; Marty et al., 2023). It has been shown that acoustic emissions reproduce many characteristics of observed foreshock sequences, including a migration towards the hypocenter of the main rupture, an inverse Omori like acceleration of AE rate (Marty et al., 2023), and a decrease of the b-value of AE before the mainshock (W. Goebel et al., 2013; Marty et al., 2023). The assumption of AE driven by aseismic slip is suggested by the low ratio between seismic and aseismic average energy release in these experiments. However, as acoustic emissions could also be triggered by cascading stress transfers independent of aseismic slip, the detailed dynamics of aseismic slip remains largely unknown. Inverting the evolution of aseismic slip during such a nucleation stage could aid in comprehending its dynamics, and its relationship with acoustic emissions.

In this paper, we make the attempt to invert the evolution of fault slip during the nucleation phase of laboratory earthquakes, using strain gauge measurements. We first computed the Green's functions of the fault system using the 3D finite element method and used these functions to invert the fault slip resulting from the spontaneous nucleation of an instability along the experimental fault. For that we use a specific parametrization to reduce the non-uniqueness of the problem, as suggested by previous studies focusing of real faults. We show that the inversion of the experimental data highlights the growth of a slip patch along the fault during the nucleation of laboratory earthquakes. This new method opens the doors to fault slip imagery at the laboratory scale, allowing a better description of the transient phenomena during the seismic cycle in the laboratory, which will improve our understanding of the mechanical control on aseismic slip development.

2 Dataset: aseismic nucleation of laboratory earthquakes

We consider here stick-slip experiments performed in a tri-axial cell in the laboratory. In this section, we provide a short summary of the experimental setup and results.

A cylindrical saw-cut Westerly Granite sample was first loaded in a tri-axial cell located in ESEILA (Experimental SEIsmology LAboratory, Géoazur, Nice). The faults surfaces were polished using a silicon carbide powder with grains having a 5-µm diameter (equivalent to #1200 grit). The fault presents an angle of θ of 30^o with respect to the applied axial stress σ_1. Experiment was conducted at 90 MPa confining pressure, imposing a constant volume injection rate in the axial chamber. The experiment resulted in the spontaneous nucleation of 5 events (Figure 1a). During the whole experiment, the shortening of the sample was monitored using three gap transducers located outside of the cell. In addition, an array of strain gauges (G1 to G8) also measured the evolution of local strain (inset in Figure 1b). Each strain gages is composed of one resistors ($\Omega =$ 120 ohms), presenting an accuracy in measurement of about 1 $\mu\epsilon$. Strain gauges were distributed around the fault (Figure 1b), about 2.4 mm from it, and measured preferentially the strain ε_{11} (Figure 1b) in the direction of the principal stress σ_1, as presented in Figure 1b. In the latter, both slip and axial strain measurements will be used in the inversion procedure. All measurements were recorded at a sampling rate of 2400 Hz during the entire experiments, using an acquisition system developed by HBM company.

By utilizing these measurements, we can estimate the elastic constants of the rock during the elastic phase of the experiments and adjust the externally measured shortening for the apparatus's rigidity using the following equation:

$$\varepsilon_{ax}^{FS} = \varepsilon_{ax}^{sample} + \frac{\Delta\sigma}{E_{ap}} \tag{1}$$

where ε_{ax}^{FS} is the average axial strain measured on gap sensors, $\varepsilon_{ax}^{sample}$ is the axial strain of the sample measured by the strain gages, $\Delta\sigma$ is the differential stress ($\Delta\sigma = \sigma_1 - P_c$) and E_{ap} is the rigidity of the apparatus. The rigidity of the apparatus ranges between 25 and 40 GPa depending of the applied load. By applying the principles of linear elasticity, strain measurements can effectively estimate the local static stress changes during experiments. The axial shortening is measured by external capacitive gap sensors and combined with axial strain gauge data to estimate the axial displacement as follows:

$$\delta_{ax} = \varepsilon_{ax}^{sample} L = \left(\varepsilon_{ax}^{FS} - \frac{\Delta\sigma}{E_{ap}}\right) L \tag{2}$$

where L is the length of the rock sample. The spatial average of displacement along the fault during the experiments can then be estimated by projecting this value as $\delta_m = \delta_{ax}/\cos\theta$, where θ is the angle of the fault compared to σ_1. The gap sensors allow an accuracy of 0.1 μm on δ_m.

Stick-slip events were all preceded by a nucleation phase, characterized on the strain measurements by a deviation from elasticity (deviation from the linear trend shown as black dotted lines in Figure 1a), suggesting that inelastic processes occur along the fault before the mainshock. The nucleation phases of events 1 to 4 are highlighted in Figure 1a by the yellow and red patches labeled Evt1, Evt2, Evt3 and Evt4 respectively. In the following sections, we design a method to invert the fault slip history during these nucleation periods and we detail the results obtained for Evt4. This event occurs at $t =$ 367 seconds exactly, and the departs from linearity on the first strain gauge is observed at approximately $t = 322$ seconds (1a).

3 Method: kinematic slip inversion for the nucleation of stick-slip events in saw-cut samples

The setup we intend to model in this study is a typical rock-mechanics setup consisting of a cylindrical saw-cut rock sample loaded in a tri-axial cell (Figure 1b). The rock sample is modeled as an elastic cylinder of height $h = 8.56$ cm, radius $a = 1.98$ cm, under confining pressure $\sigma_3 = P_c = 90$ MPa and axial load σ_1 (Figure 1b). The Young's modulus is noted E and the Poisson ratio ν (table 1). The sample is saw cut at angle θ with the (vertical) axial load, creating an elliptical fault Σ. In this section, we use the Cartesian coordinate system associated to the principal stresses $(\vec{e}_1, \vec{e}_2, \vec{e}_3)$ shown in Figure 1b. As the load increases, slip δ is initiated on the fault. It is defined as the displacement discontinuity across the fault plane Σ:

$$\vec{\delta}(\vec{\xi}, t) = \vec{u}(\vec{\xi}^{+}, t) - \vec{u}(\vec{\xi}^{-}, t), \tag{3}$$

where $\vec{u}$ is the displacement field, $\vec{\xi}$ the position along the fault and t time. Superscripts $+$ and $-$ refer to the two sides of the fault. Because of the geometry of the sample and the loading device, we assume that slip only occurs within the fault plane (no opening), in the direction of the great axis of the ellipse, so that:

$$\vec{\delta}(\vec{\xi},t) = \delta(\vec{\xi},t)\vec{x}_1, \tag{4}$$

where $\vec{x}_1$ is a unit vector tangent to the fault plane (Figure 1b). The no opening assumption is relevant here since the fault is a smooth interface under high normal stress. As mentioned in the previous section, 8 strain gauges are distributed along the fault (Figure 1b) and continuously measure the strain component ε_{11} related to fault reactivation. Note that the index 1 refers here to the vector $\vec{e}_1$ in Figure 1b (the strain gauges were specifically oriented to measure elongation or shortening in this direction). Displacement sensors allow to monitor the sample shortening, that can be used to estimate the average fault slip history. Here we derive a method to image the slip evolution on the fault from the strain and average slip measurements, relying on a Green's function approach. For that we consider the static equilibrium of the lower-half sample (i.e. the part of the sample situated below the fault as show in Figure 1b). In this domain, delimited by the surfaces S_b, S_l and Σ (Figure 1b), the stress components satisfy:

$$\sigma_{ij,j} = 0. \tag{5}$$

The rock being elastic, the stress components σ_{ij} are related to the strain components ε_{ij} with the Hooke's law:

$$\sigma_{ij} = \frac{E\nu}{(1+\nu)(1-2\nu)}\delta_{ij}\varepsilon_{kk} + \frac{E}{(1+\nu)}\varepsilon_{ij}. \tag{6}$$

The strain components relate to the displacement components as:

$$\varepsilon_{ij} = \frac{1}{2}\left(u_{i,j} + u_{j,i}\right). \tag{7}$$

We also assume the following boundary conditions, guided by the experimental setup:

$$\begin{cases} \vec{u} &= \vec{0} \quad \text{on} \quad \vec{x} \in S_b \\ \vec{T} &= -P_c\vec{e}_r \quad \text{on} \quad \vec{x} \in S_l \\ \vec{u} &= \frac{1}{2}\delta\vec{x}_1 \quad \text{on} \quad \vec{x} \in \Sigma. \end{cases} \tag{8}$$

where $\vec{T}$ (Pa) is the traction on the lateral boundary of the domain,and $\vec{e}_r$ is the unit radial vector of the cylindrical coordinate system related to the sample (Figure 1b). The sample is fixed at the bottom (S_b no displacement), undergoes a constant confining pressure P_c (Pa) on the lateral boundary S_l. Slip δ (m) is prescribed on the fault Σ in the direction $\vec{x}_1$. The 1/2 factor appearing in the third equation of (8) arises from the symmetry of the rock sample with respect to the fault plane. To compute the Green's functions necessary for our problem, we prescribe the following unit slip distribution on the fault:

$$\delta = A\delta_D(\vec{\eta} - \vec{\xi}), \tag{9}$$

where δ_D is the Dirac delta function, $\vec{\xi}$ is the position of a point on the fault, $\vec{\eta}$ is the position of a point in the $(\vec{e}_1, \vec{e}_2, \vec{e}_3)$ space, and A a constant ($A = 1m^3$). The Green's function $G(\vec{\xi}, \vec{\eta})$ is then obtained as the ε_{11} component of the strain tensor satisfying (5) in the lower-half sample, assuming (6), (7), (8) and (9). Note that G has units of strain per meter. By superposition, the strain ε_{11} for a general distribution of slip δ along the fault is then given by:

$$\varepsilon_{11}(\vec{\eta},t) = \int_{\Sigma} G(\vec{\xi},\vec{\eta})\delta(\vec{\xi},t)d^2\vec{\xi}. \tag{10}$$

The average slip δ_m writes:

$$\delta_m(t) = \frac{1}{\Sigma_0} \int_\Sigma \delta(\vec{\xi}, t) d^2\vec{\xi}, \tag{11}$$

where Σ_0 is the measure of the fault surface Σ. Equations (10) and (11) are our forward problem, relating the slip distribution (δ) to the observables ε_{11} and δ_m. Note that the forward problem is linear as long as the parameters considered are the values of δ at a specific position $\vec{\xi}$ along the fault and time t. As shown later, we will however use a different parametrization making the inverse problem non-linear. The static problem (5) is solved with a 3D finite element approach. For that we used the MATLAB Partial Differential Equation Toolbox (Inc., 2023). We discretize the domain Ω into $N_e = 52576$ quadratic tetrahedral elements, so that the fault surface contains 3137 nodes. The typical spacing between nodes is between 1 and 2 mm. The Green's functions $G(\vec{\xi}, \vec{\eta})$ can then be obtained by solving the static equilibrium problem, for positions $\vec{\xi}$ corresponding to each N_f node of the fault. However, the large number of fault nodes (3137) would make the inversion of fault slip not tractable, or poorly constrained, as we are interested in inferring slip history at each node location. To reduce the number of parameters, we use in the inversion process a coarser triangular mesh for the fault, consisting of $N_f =$ 24 nodes. We therefore only solve the static problem for the 24 $\vec{\xi}$ values of the coarse grid. Doing so, the imposed slip on the fault is first bi-linearly interpolated on the finer mesh, involving 3137 nodes. Note that in the finite elements approach used here, imposing unit slip on one node (with vanishing elsewhere) corresponds to consider a quadratic slip distribution with a compact support, made of the elements connected to the slipping node. It is this quadratic function that is interpolated on the finer grid, before solving the static problem. The choice of 24 nodes is a compromise between the resolution (discussed in the next section) and the number of parameters to be inverted. These Green's functions are finally evaluated at the N_g positions $\vec{\eta}_g$ of the strain gauges, and stored in a $(N_g \times N_f)$ matrix $\mathbf{G}$. We have:

$$\mathbf{G}_{ij} = G(\vec{\xi}_j, \vec{\eta}_{gi}), \quad i = 1, ..., N_g \quad j = 1, ..., N_f. \tag{12}$$

Before using the Green's function in the inversion process, we determined the minimum mesh size necessary to achieve a reasonable accuracy of the Green's functions. For that we considered the same coarse fault mesh, and computed the Green's function for different meshes in the bulk sample. The dependence of the Green's function on the bulk mesh size is shown in the supplementary material (Figures S3, S4 and S5). Overall, the Green's functions are stable for bulk mesh sizes lower than about 3 mm. We therefore used a bulk mesh size between 0.75 and 1.5 mm to compute the Green's functions. As shown in the supplementary material, the accuracy achieved is between 10^{-6} and 10^{-5} strains, depending on the components.

The strains ε_{11} at positions $\vec{\eta}_g$ and the slip δ at the fault nodes are also stored into a $N_g \times 1$ vector $\mathbf{S}$, and a $N_f \times 1$ vector $\mathbf{U}$ respectively. Thus, equation (10) becomes:

$$\mathbf{S}(t) = \mathbf{GU}(t). \tag{13}$$

Similarly, equation (11) could be written as:

$$U_m(t) = \mathbf{M}^T \mathbf{U}(t), \tag{14}$$

where $U_m(t)$ is the value of average slip at time t, the vector $\mathbf{M}$ ($N_f \times 1$) is the spatial average operator, and T denotes the transpose. Imaging the fault slip evolution $\delta(\vec{\xi}, t)$ thus reduces to infer $N_f \times N_t$ parameters, where N_t is the total number of strain measurements on one strain gauge, or the number of time steps considered. The number of observations is $(N_g+1) \times N_t$. Since $N_g < N_f$, the problem is largely under-determined.

In order to reduce the number of unknown parameters, we follow the parametrization proposed by Liu et al. (2006) for the kinematic coseismic slip inversion of the 2004 Parkfield earthquake. Namely, the slip history at node j (U_j) is parametrized as:

$$U_j(t) = \begin{cases} 0 \quad \text{if } t < t_{0j} \\ \frac{1}{2}\Delta u_j \left[1 - \cos\frac{\pi(t-t_{0j})}{T_j}\right] \quad \text{if } t_{0j} < t < t_{0j} + T_j \\ \Delta u_j \quad \text{if } t > t_{0j} + T_j \end{cases} \tag{15}$$

From equation (15), the fault slip at node j is identically zero before an arrival (onset) time t_{0j}, then reaches a maximum value Δu_j over the rise time T_j. After that, it remains constant at Δu_j. The cosine function used here implies a smooth transition from zero slip to Δu_j. Doing so, we reduce the number of unknown parameters from $N_t \times N_f$ to $3N_f$. We therefore define a $(3N_f \times 1)$ parameter vector $\mathbf{X}$ as:

$$X_k = \begin{cases} \Delta u_k \quad \text{if } k = 1, ..., N_f \\ t_{0k} \quad \text{if } k = N_f + 1, ..., 2N_f \\ T_k \quad \text{if } k = 2N_f + 1, ..., 3N_f \end{cases} \tag{16}$$

The inverse problem then consists of finding $\mathbf{X}$ minimizing the objective function J defined as:

$$\begin{aligned} J(\mathbf{X}) \quad = \quad & \frac{1}{2}\sum_k \left[\mathbf{S_0}(t_k) - \mathbf{G}\mathbf{U}(t_k, \mathbf{X})\right]^T \mathbf{C_{ds}}^{-1} \left[\mathbf{S_0}(t_k) - \mathbf{G}\mathbf{U}(t_k, \mathbf{X})\right] \\ & + \frac{1}{2}\sum_k \left[U_{m0}(t_k) - \mathbf{M^T}\mathbf{U}(t_k, \mathbf{X})\right]^T C_{du}^{-1} \left[U_{m0}(t_k) - \mathbf{M^T}\mathbf{U}(t_k, \mathbf{X})\right] \\ & + \lambda \left(\nabla \mathbf{X}\right)^T \left(\nabla \mathbf{X}\right), \end{aligned} \tag{17}$$

where $\mathbf{S_0}(t_k)$ is a $(N_g \times 1)$ vector containing the values of ε_{11} at the gauges positions and time t_k, $U_{m0}(t_k)$ the observed mean slip on the fault at time t_k, and λ a regularization parameter. The regularization here consists of minimizing the gradient norm of the parameters $\mathbf{X}$, to favor smoothly varying parameters with position along the fault. $\mathbf{C_{ds}}$ is the $(N_g \times N_g)$ covariance matrix for the strain data. We only consider for $\mathbf{C_{ds}}$ a diagonal matrix to represent the variances of the observed strains (calculated from the accuracy of the strain sensors 10^{-6}), ignoring the cross terms. C_{du} is the variance of the observed mean slip. The standard deviation of the strain measurements (related to the noise in the sensors) is less than 10^{-6}, and 0.1 μm for the mean slip. In order to account for the limitations of the forward model (homogeneous medium, quasi static approximation, fully rigid boundary condition on the bottom boundary of the sample), we first increased these values by an amount obtained from the final RMS of a first inversion, that is 0.76×10^{-6} for the strain, and 0.2 μm for slip. Then, we had to account for the quality of the gauges, that could be estimated by their ability to capture the elastic deformation of the sample, before the onset of slip on the fault. This gauge quality was computed as the ratio $\varepsilon_{ax}^{G_i}/\varepsilon_{ax}$, corresponding to the ratio between the strain measured by each strain gauge G_i during the elastic loading, and the axial strain measured via the gap sensors ($\varepsilon_{ax} = \varepsilon_{ax}^{FS} - \frac{\Delta\sigma}{E_{ap}}$, see part 2 for details). We therefore weight each component of C_{ds} by a factor between 0 and 1, where 0 means the gauge does not record any elastic signal, and 1 the gauge records the maximum elastic signal. The diagonal components of C_{ds} given in table 2 finally range between 0.33×10^{-11} and 0.89×10^{-11}. Similarly, we get $C_{du} = (0.3)^2$ $(\mu\text{m})^2$. We also normalized the strain and slip measurements ($\mathbf{S_0}$ and U_{m0}) by the maximum magnitude of all the strain time series and the mean slip time series, noted ε_0 and δ_0 respectively. Accordingly, the slip vector $\mathbf{U}$ is normalized by δ_0, and each row of the matrix $\mathbf{G}$ by ε_0/δ_0. Time was also normalized by the duration of the measurement time series t_{max}, so that our parameter vector $\mathbf{X}$ was normalized using δ_0 and t_{max}. Accordingly, we normalized C_{du} and each component of $\mathbf{C_{ds}}$ by δ_0^2 and ε_0^2.

Sample height (RP) h	8.56 cm
Sample section radius (RP) a	1.98 cm
Fault angle θ w.r.t principal stress (RP)	30°
Young's modulus (RP) E	65 GPa
Poisson ratio (RP) ν	0.25
Confining pressure (RP) P_c	90 MPa
Number of elements for Green's function computation (MP) N_e	52576
Number of nodes on the fault for Green's function computation (MP) N_f^0	3137
Number of nodes on the fault for inversion (IP) N_f	24
Standard deviation of strain measurements (IP)	10^{-6}
Standard deviation of mean slip measurements (IP)	0.1 μm
Regularization parameter (IP)λ	10^{-6}-10^{2}

Table 1. Rock sample properties (RP), mesh properties (MP) and inversion parameters (IP).

Gauge number	quality factor	C_{ds}^{-1}
1	0.920	0.3441×10^{-11}
2	0.755	0.4196×10^{-11}
3	0.890	0.3557×10^{-11}
4	1	0.3168×10^{-11}
5	0.778	0.4068×10^{-11}
6	0.355	0.8918×10^{-11}
7	0.836	0.3787×10^{-11}
8	0.958	0.3306×10^{-11}

Table 2. Gauge quality factor and C_{ds} components

The optimization of the objective function is performed with a BFGS (Quasi-Newton-Broyden Fletcher-Goldfarb-Shanno) algorithm (Broyden, 1970; Fletcher, 1970; Goldfarb, 1970; Shanno, 1970; Fletcher, 1982). The optimization step results in a first estimation of the best model of fault slip. In order to estimate the uncertainty on the fault slip distribution, we conduct in a second step a probabilistic inversion. For that we use the outcome of the first inversion step as an initial model in a Metropolis-Hasting algorithm (application of the Markov Chain Monte Carlo (MCMC) methods (Metropolis et al., 1953; Hastings, 1970)), allowing to sample the posterior distribution of the model parameters $\mathbf{X}$. Using the best model from the BFGS algorithm to initiate the Bayesian inversion reduces the duration of the burn-in phase in the MCMC exploration.

In the next sections, we perform a resolution analysis of our inverse problem, and discuss synthetic tests to evaluate the performance of the deterministic part of the kinematic inversion method. Then we present the application to the experiment described in the previous section and Figure 1a. In both sections, we consider the same rock material: the granite sample characterized by the properties listed in table 1. Table 1 also summarizes the computational parameters used in the following.

4 Resolution analysis

As illustrated in Figure 1a and 1b, the strain gauge array used in the experiments is located on the outer ream of the fault, on the sample edges. Since the stress (and thus strain) field associated with a growing crack decreases as an inverse power of the distance to the crack tip (Lawn, 1993), we expect strain gauges to be less sensitive to slip occurring on the central part of the fault. To quantify this, we calculate the resolution matrix **R** for our problem (Tarantola, 2005) as follows:

$$\mathbf{R} = \mathbf{G}^T \mathbf{C}_{ds}^{-1} \mathbf{G} + C_{du}^{-1} \mathbf{M}\mathbf{M}^T. \qquad (18)$$

The normalized diagonal elements r_i of **R** are represented in Figure 2a. It clearly indicates that fault regions situated at more than a few cm away from the gauges are poorly resolved, and thus if slip occurs it may not be correctly mapped to these parts of the fault (Radiguet et al., 2011; Twardzik et al., 2021). Note also that nodes situated very close to strain gauges dominate the resolution (r_i is about two times larger there than elsewhere on the fault). In the following, we will separate fault regions with non zero resolution from non resolved areas by drawing the line ($r_i = 0.05$) (heavy red dashed line in Figure 2).

An important issue for the application presented in the next section, is the reliability of inverted slip in the central region of the fault. Therefore, we show in Figures 2b to 2i the restitution ρ_k of the eight nodes located in this area. The restitution ρ_k corresponds here to the k^{th} line of the resolution matrix R, and indicates to what extent slip on the k^{th} node might be wrongly assigned to other nodes on the fault, possibly with opposite direction (leading to negative values) (Radiguet et al., 2011; Twardzik et al., 2021). For six nodes out of the eight nodes considered, the restitution is maximum at the node concerned, even if it is somewhat leaking on the closest nodes. Slip on these nodes can therefore eventually be attributed to neighboring nodes, but it can not be wrongly assigned to other remote regions of the fault. The two exceptions concern the nodes situated at ($x_1 \simeq -2.5$ cm, $x_2 \simeq 0$ cm) (Figure 2b) and at ($x_1 \simeq -0.5$ cm, $x_2 \simeq -0.75$ cm) (Figure 2h). If slip occurs at these nodes, the array might not be able to correctly locate it, and attribute slip to the neighboring nodes.

The resolution analysis discussed here motivates the use of a regularization (smoothing) term in the definition of the objective function (17), that can limit the effects of poor resolution.

5 Synthetic test with elliptical shear crack growth

We next generate synthetic data using the Green's functions **G** from a slip distribution δ corresponding to an elliptical crack of aspect ratio α growing from the fault center with constant rupture speed v_r and stress drop $\Delta\tau$. The slip distribution is given by:

$$\delta(\vec{x}, t) = \begin{cases} \frac{\Delta\tau}{\mu}\sqrt{v_r^2 t^2 - x_1^2 - (\alpha x_2)^2} & \text{if } x_1^2 + \alpha^2 x_2^2 < v_r^2 t^2 \\ 0, & \text{if } x_1^2 + \alpha^2 x_2^2 \geq v_r^2 t^2 \end{cases} \qquad (19)$$

where x_1 and x_2 are the coordinates within the fault plane (Figure 1b), and $\mu = E/2(1+\nu)$ the shear modulus. In these tests, $\alpha = 2$, which is the aspect ratio of the experimental fault. We considered $v_r = 4{\times}10^{-4}$ m.s^{-1}, so that the crack front reaches the edges of the fault after $t_{max} = 100$ s, and a stress drop $\Delta\tau = 2.6$ MPa. The other parameters used are listed in table 1. The strain component ε_{11} and the spatial average of slip are used as data $\mathbf{S_0}$ and U_{m0} in our inversion procedure. We also added 5% of Gaussian noise on the synthetic strain and average slip data. We start from an initial model where Δu, t_0 and T are constant on the fault.

Then, we perform the inversion of the synthetic data for two different virtual observational networks, hereafter labeled SGA1 (strain gauge array 1) and SGA2 (strain gauge array 2) involving $N_g = 16$ and $N_g = 10$ strain gauges respectively. In SGA1, gauges are all situated 2.4 mm below the fault, and evenly distributed in the whole fault area. Gauges locations are not restricted to the outer ream of the fault. SGA2 consists of 10 gauges located all around the fault, but at different distances from it. In SGA1 and

SGA2, gauges are considered perfect, with quality factor 1, so that C_{ds} components are all equal to the fourth component given in table 2. We also consider a case with the gauges distribution used for the real experiment of the next section (RSG, $N_g = 8$). For each gauge distribution, we also considered 9 different values of the regularization parameter λ ranging from 10^{-6} to 10^2. The inverted slip distribution, and the comparison between strain data and inverted model predictions are shown in Figures 3, 4 and 5. In these Figures, we present the results obtained with $\lambda = 10^{-1}$ (this choice will be justified later in this section).

For a dense distribution of strain gauges ($N_g = 16$) covering the whole fault area, the slip distribution is reasonably well retrieved (Figure 3 second row, Figure 4), with a satisfactory fit between the synthetic strain data and the simulated strain (Figure 5). The propagation of a slip front from the center of the fault is clearly identifiable. As the strain gauges distribution becomes sparser (RSG and SGA2), the inversion procedure has more difficulties in retrieving the synthetic model (third and fourth row in Figure 3, Figure 4), although the synthetic strain data are reasonable well reproduced (third row in Figure 5). Placing the gauges away from the fault (SGA2) even makes the inversion result worse, although the number of sensors is the same as in RSG. The correct amount of total slip is predicted by the inverted model, but instead of retrieving a crack like pattern at $t = 100$s, the inverted slip is more diffuse. We interpret this feature as a consequence of the rapid decay of strain changes away from the crack front. It is thus important to keep strain gauges close to the fault. In the case of the real strain gauge array (RSG), the inversion has a tendency to miss slip at the node situated at ($x_1 \simeq -0.5$ cm, $x_2 = -0.75$ cm), and to compensate by increasing slip on the neighboring nodes. This is particularly clear at $t = 50$ s and $t = 75$ s. This feature was already suggested by the resolution analysis, indicating a poor restitution for this node (Figure 2h). Residual slip is also wrongly assigned at the left and right edges of the fault, in regions characterized by a poor resolution (shaded areas in the last row of Figure 3, reporting the resolution of 2a). Finally, slip is underestimated in the low resolution zone of the central region of the fault ($0 < x_1 < 2$ cm).

Note that the high frequency component of strain changes is not always well retrieved by the inversion, even for a dense strain gauge array. This feature is well illustrated in Figure 5, panel G4 of the first line (SGA1): the abrupt change and peak in strain at $t = 35$ s associated with the crack front are not retrieved. We attribute this to the parametrization used for the inversion (implying a smooth cosine function), to the regularization or to a local mimimum of the objective function. However, as shown later, the experimental data used do not exhibit such rapid variation of strain, so that our parametrization should not affect the quality of the data fitting.

As shown in the supplementary material, the results of this synthetic test do not depend on the level of noise added to the synthetic data, at least in the range 0 to 10 % of Gaussian noise (Figures S7 and S8).

In order to further quantify the performance of our inversion method, and to identify the most relevant value of the regularization parameter λ, we calculate the RMS distance between the synthetic model (19) and the inverted models, as:

$$RMS = \sqrt{\frac{1}{N_f N_t} \sum_k \left[\mathbf{U}_i(t_k) - \mathbf{U}_s(t_k)\right]^T \left[\mathbf{U}_i(t_k) - \mathbf{U}_s(t_k)\right]}, \tag{20}$$

where $\mathbf{U}_s$ and $\mathbf{U}_i$ are the synthetic and inverted slip vectors at time t_k (the synthetic slip is obtained using equation (19)). N_f and N_t are the number of nodes on the fault and the number of time steps considered. The RMS dependence on the regularization parameter λ and the number of gauges N_g is shown in Figure 6a, along with the minimum value of the objective function reached during the inversion iterations (L-curve) in Figure 6b. First, the RMS (Figure 6a) is essentially dependent on the number of strain gauges used in the inversion: it decreases roughly by a factor of two when the number of strain gauges is increased by the same factor (RSG vs. SGA1). Then, for a given configuration of strain gauges, the RMS is approximately constant (or slightly decreasing) for a wide range of λ values, and only increases at large λ. This latter tendency is also true for the objective function (Figure 6b), indicating the maximum value of λ one can use confidently without altering the fit to observations (and the RMS in the case of the synthetic test). As long as $\lambda \leq 10^{-2}$, it has a limited influence on the RMS (Figure 6a), and does not drastically modifies the performance of the inversion (Figure 6b). For the real strain gauge network ($N_g = 8$), when $\lambda \leq 10^{-2}$ the RMS is such that the synthetic model is retrieved with a typical error of 4 μm. For denser strain gauges, the RMS error could be reduced to 1μm, provided that the number of gauges is large enough (yellow symbols in Figure 6a). For $\lambda > 10^{-2}$, the smoothing constrain becomes significant (Figure 6b), resulting in much higher values of the objective function. Based on the results of Figure 6b, we therefore choose in the following $\lambda = 10^{-1}$ as the best compromise, since some smoothing is needed to balance the low resolution offered by the strain gauge array.

In the supplementary material, two additional synthetic tests are shown, attempting at retrieving a Gaussian slip distribution of various size, either centered on a node or between two nodes (Figures S9 to S12). These tests provide additional constraints on the ability of the inversion to resolve slip on the fault. It is shown that when the Gaussian is centered on a node, the method has no difficulty to detect a slip patch, even with a length scale smaller than the typical inter-node distance. However, if the maximum of slip is located between two nodes, the true slip pattern is badly captured as long as its typical length scale is smaller than about 0.47 cm (half the typical inter-node distance). Since the probability of nucleating an arbitrary slip event exactly on a node location in a real experiment is negligible, we take this value (0.47 cm) as an order of magnitude for the minimum length scale that can be resolved in the inversion. Recall that this value is essentially controlled by the mesh size used in the inversion.

A third series of tests considers a bimodal Gaussian slip distribution with varying distance between the maxima (Figures S13 to S18). The bimodal shape is only retrieved by the inversion when the Gaussian maxima are separated by more than one centimeter from each other (Figures S13 to S18), but because of the poor resolution between gauges G2 and G3, one of the maximum is wrongly located in the middle of the fault. We conclude that the method could in principle resolve two distinct slipping patches, as long as they are separated by more than a centimeter, and situated in a region with reasonable resolution.

6 Application on the nucleation of a laboratory earthquake

We now apply the kinematic inversion procedure on the experimental results described in section 2, and shown in Figure 1b. Using this data set, we performed a kinematic inversion of the nucleation period of Evt4 shown in Figure 1a (between 322 s and 367 s).

Following the methodology detailed in section 2, we proceeded in two steps. First we used the deterministic approach to obtain the model minimizing the objective function J given in equation (17). Then we used this result as an initial model in the probabilistic (MCMC) approach. We performed 10^8 steps for the MCMC algorithm, resulting in an acceptance rate of 0.25. For the MCMC step, we used the non-regularized objective function (equation (17) with $\lambda = 0$). We also restricted the MCMC exploration between 0 and $4\delta_m^{max}$ for Δu, between 0 and t_{max} for t_0 and between 0 and $4t_{max}$ for T, δ_m^{max} and t_{max} being the maximum average fault slip and the duration of the observation window. The onset time t_0 can not by definition exceed t_{max}. Δu and T can however be arbitrarily large, in order to allow for ever accelerating slip on the fault during the observation window. The bounds on Δu and T were chosen large enough to capture late acceleration, but small enough to make the MCMC algorithm converge. This choice will be further discussed later. The result of the second step is a posterior Probability Density Function for each parameter (each component of $\mathbf{X}$). The joint PDFs are presented in the supplementary material (Figures S21, S22 and S23). Before computing the PDFs, we removed the 6×10^6 first models corresponding to the burn-in phase in the MCMC chain. In order to translate these results in terms of slip and slip uncertainty, we reconstructed the slip history for each model $\mathbf{X}$ in the MCMC chain following equation (15). From that we derived the mean and standard deviation of slip at any time and any given position along the fault.

The results of the deterministic step for Evt4 are presented in Figures 7 and 8. Figures 9, 10, 11, 12, 13, 14 and 15 show the outcome of the MCMC step.

The best model resulting from the deterministic step (Figure 7) shows the nucleation of a slip event on a small patch situated in the top central part of the fault, starting at about $t = 11s$. This slipping patch later expands to the left, then to the lower part of the fault, resulting in a crack like pattern after 44 s, with a maximum slip of 3.5 μm (last panel in Figure 7). The mean slip rate during the experiment is thus about 0.08 μm.s^{-1}, a typical value for slow aseismic slip (Avouac, 2015).

The expansion of the slipping patch is of the order of a few centimeters in 45 s, that is between 10 to 100 m per day. The propagation speed of the slip events observed in the experiment will be further discussed later (Figure 16).

Note however that a significant part of this slip event affects a fault region with poor resolution (between $x_1 = 0$ and $x_1 = 2$ cm). The maximum of slip at the end of the observation window is located on the two nodes within this poor resolution area. Based on the restitution calculated for these particular two nodes (Figures 2e and 2g), the location of this slip maximum is probably not a robust feature, and could either be shifted on neighboring nodes, or smoothed over the central part of the fault. Furthermore, between $t = 22.49$ s and $t = 37.49$ s, the slip pattern seems to avoid the node situated at ($x_1 \simeq -0.5$ cm, $x_2 = -0.75$ cm). This pattern was also generated by the inversion on the synthetic data, instead of an elliptical growing crack. Based on the restitution of this particular node (Figure 2h), we conclude again that the U-shaped slip distribution is not reliable, and might correspond to a more simple distribution of slip. The last feature that has to be taken with care is the activation of the three nodes situated at the left and right edges of the fault (close to strain gauges G3 and G6), from $t = 11.24$ s and $t = 29.99$ s. The three nodes are once again poorly resolved (Figure 2a), as they are the three boundary nodes the farther away from a strain gauge. It has been shown in the synthetic test that the inversion can wrongly attribute slip on these nodes.

As shown in Figure 8, the inverted model provides a satisfactory fit to the strain and average slip measurements, at least up to 40 s, where average slip tends to be slightly underestimated by the best model. Late strain predictions ($t > 40$ s) also deviates from the observations. These discrepancies could be related to the regularization term that does not allow to obtain the smallest possible objective function (Figure 6b). It could also be a sign that the BFGS algorithm converged to a local minimum of the objective function. In order to quantify the quality of the fit, we computed the RMS_i between data and best deterministic model predictions as:

$$RMS_i = \sqrt{\frac{2J}{N_g N_t}}, \tag{21}$$

where J is the objective function defined in equation (17), and evaluated for the best model, N_g is the number of strain gauges and N_t is the number of time steps. In computing the RMS, we assumed a regularization parameter $\lambda = 0$. We obtained a $RMS_i = 0.558$

for this deterministic step. This value corresponds to $J/N_g \simeq 700$, in the upper range of what was obtained during the synthetic tests (Figure 6).

These first results motivate the need for a more global exploration of the parameter space, and a quantitative assessment of the uncertainty on the slip distribution. We therefore performed in a second step the MCMC Bayesian inversion. The range of possible slip history at each fault node reconstructed from the accepted models in the MCMC chain is illustrated in the density plots of Figure 9. These results first show that the MCMC exploration identified one main slip pattern, since the distribution of possible slip at a given time and a given node shows a single maximum. The only node showing two maxima is node 3, situated in a low resolution region of the fault plane, already identified in the previous sections. Overall the nodes situated in low resolution areas are characterized by an important uncertainty on the slip amount at each time step.

The mean reconstructed slip distribution has a slightly different pattern than the best deterministic model prediction (Figure 10). Once again, we obtain an aseismic slip event nucleating between $t = 10$ s and $t = 20$s, before propagating in the central region of the fault. However slip initiates closer to the left edge of the fault, and the slipping patch essentially propagates to the right. The slip maximum is larger than what was predicted by the best deterministic model, and occurs close to the initiation location (node 19, $x_1 \simeq -2.7$ cm, $x_2 \simeq 0$ cm). As before, part of the slip event affects poorly resolved areas of the fault, but interestingly, less slip occurs in the low resolution area at the right end of the fault.

The slip rate evolution along the fault, computed from the mean reconstructed slip is shown in Figure 11. Slip rate increases to approximately 0.25μm.s^{-1} in the region of node 19 until $t \simeq 15s$. Slip rate then remains constant in this area between $t = 15s$ and $t = 38s$, before decreasing, while another patch starts to slip at about 0.25μm.s^{-1} in the right region of the fault after $t = 40s$. This feature highlights the expansion of the slipping region to the right. Overall the slip rate distribution is coherent with an expanding crack pattern, with high slip rate in the slip front region, and non-vanishing slip rate on the whole slipping patch.

The Bayesian approach also provides estimates of the slip uncertainty, as evaluated from the predictions of the MCMC chain. Overall, when considering the full space time evolution of fault slip, the resulting standard deviation on slip σ_δ ranges between 0 and 3.2 μm, with a mean value of 0.28 μm (Figure 13). Figure 12 shows σ_δ maps at different time steps. The left end region of the fault is characterized by the highest uncertainty that increases up to 3.2 μm as the slip event develops on the fault. Another region of high σ_δ is the central right region, with a local maximum of σ_δ reaching 2.5 μm at the end of the observation window (last panel in Figure 12). Elsewhere on the fault, the uncertainty does not exceed 1.5 μm. Importantly, the maxima of σ_δ are located within low resolution zones, outlined by the shaded zones in Figure 12, indicating that the distance to strain gauges is the main limitation to image accurately slip on the fault.

The mean model resulting from the Bayesian inversion improves the fit to the observation (Figure 14), compared to the best model resulting from the deterministic step. In particular, the higher amount of fault slip allows a better agreement on average slip after 40 s. Moreover, the models accepted during the MCMC iterations predict strain and slip evolutions within the uncertainty on the measurements (a zoomed version of Figure 14 between $t = 20$ s and $t = 24$ s is provided in Figure 15). As for the deterministic step, we computed the RMS_i value for each of the model accepted during the MCMC exploration, following equation (21). The results are shown in Figure S19 of the supplementary material. Overall, the models accepted have a RMS_i ranging from 0.35 to 0.5, which is 20 % to 40 % smaller than the best deterministic model. The model resulting from this first inversion step therefore likely corresponds to a local minimum of the cost function, which justifies the need for a more global exploration, performed by the MCMC step. In order to assess the ability of the MCMC step to perform a global exploration, we ensured that the MCMC exploration did not converge to a different chain when starting from a different initial model (Figure S20 of the supplementary material).

In order to assess the occurrence of propagating aseismic slip along the fault during Evt4, we computed for each node the time $t_{2.0}$ at which slip exceeds 2.0 μm. $t_{2.0}$ is represented in Figure 16a (map view) and as a function of the distance to the node accumulating the largest slip (node 19) at the end of the observation window. The error-bars are here derived from the Baysesian inversion. To the first order, the evolution of $t_{2.0}$ with distance to the maximum slip location is consistent with an aseismic slip front propagating at a speed of the order of 200 m.day^{-1}.

The results of this inversion and the synthetic tests conducted before, although affected by a very low resolution and possible artifacts, are to some extent promising. With a denser strain gauge array, our method could constrain the spatial and temporal evolution of the slip patch during the nucleation of laboratory earthquakes.

7 Discussion: towards imaging fault slip during laboratory fault reactivation

In this work, we have tested a method to image centimetric scale aseismic quasi-static fault slip growth from local strain measurements in a tri-axial experimental setup, and to characterize the related uncertainty. Our inversion approach involves Green's function accounting for the real geometry of the saw-cut rock sample and the specificity of the triaxial loading device. The Green's functions are computed numerically with a FEM approach, where the accuracy obtained has been quantified. Beyond the numerical method, the unknown details of the granite structure introduces uncertainty in the Green's function computation. Here we simplified the rock sample as a homogeneous and isotropic medium loaded in a quasi-static manner, with rigid boundary conditions at the bottom. We balanced these simplifying assumptions by adding an epistemic component in the uncertainty on slip and strain data. However, if available, the knowledge of a detailed structure for the granite could eventually be accounted for in the FEM computation of the Green's functions.

We evaluated the capabilities of the inversion method through a resolution analysis, different synthetic tests with a prescribed slip evolution, and different configurations of monitoring arrays. We considered the strain gauge array of the real experiment (RSG) analyzed later in the manuscript, and also two virtual arrays (SGA1 and SG2). The results obtained with these three arrays suggest that using a higher number of strain gauges improves the inversion, and the best performance is obtained for gauges situated as close as possible from the fault, as anticipated by the resolution analysis (Figure 2). To go further on the question of what would be the optimal strain gauge array design, we computed the resolution matrix (equation 18) for two additional virtual arrays SGA3 and SG4 (Figure S2 supplementary material). SGA3 is inspired from new techniques of fiber-optic sensing (Rast et al., 2024) and consists of 90 gauges distributed around the fault in a similar manner as RSG (Figure S1). The high number of gauges mimics the high measurement density of fiber-optics. SGA4 is similar as RSG with additional gauges placed on the surface of the sample so as to be as close as possible from the fault center (Figure S1). We computed the resolution for SGA1, SGA3 and SGA4 using three different fault meshes, to investigate whether one of the arrays could allow to image finer details of the slip distribution. Here again, the distance to strain gauges is the main factor controlling resolution (Figure S2). SGA3 allows a high resolution on the whole external part of the fault, and would allow to refine the mesh in this region to the size $2-4$ mm. We could thus expect to decrease the minimum detectable lengthscale in this region from 46 to $2-4$ mm. The central part of the fault however, remains poorly resolved, and a finer mesh there would only increase the number of unknown parameters, and make the inversion even more under-determined. Placing additional sensors as in SGA4 does not improve the resolution with respect to RSG, whatever the fault mesh size considered. The additional gauges indeed remain too far away from the fault.

We have not investigated yet whether measuring other components of the strain tensor would improve the resolution. When considering the different components of the strain tensor at the RSG gauges location during the growth of an elliptical shear crack (Figure S6), no component dominates the signal. It is thus not obvious whether axial strain should be favored, but this conclusion could eventually be different for other sensors positions. Note also that the gauges used do not allow to measure two different components at the same position. Overall, the optimization of strain array design (strain gauge number, position, and strain component to be measured) to achieve the best resolution on fault slip evolution is an important issue, deserving more investigation.

When applying this method to a real laboratory experiment, we were able to identify some features of the nucleation process of a stick-slip event. It consists of a shear crack initiating in the left-central region of the fault, and expanding at a speed of the order of a few hundreds of m.day^{-1}, accumulating between 5 and 9 μm of slip in 45 s, representing about 8 to 15 % of the coseismic slip. The maximum slip rate during the nucleation process is about 0.25 μm.s^{-1}. Following (Lawn, 1993), the corresponding stress drop could be estimated as GV_s/V_r, where G is the shear modulus of the sample, V_s the slip rate and V_r the expansion (rupture) speed of the slipping patch. We end up with a stress drop of a few MPa, which is closer the the stress drop expected for regular earthquakes than for slow slip events (Michel et al., 2019).

Interestingly, the nucleation does not occur here as a large scale aseismic slip initiating on the whole fault, nor as a slip pulse: both the best model from the deterministic inversion and the mean model from the MCMC exploration indicate a crack like pattern, with maximum slip occurring close to the slip initiation location. A robust feature is the absence of slip before 20 s on nodes 5, 10 to 15 and 21 while significant slip occurs on node 19 (Figure 9), suggesting that the nucleation does not activate a slowly creeping fault but a locked interface.

Due to the rapid decay of strain with distance from the slipping region, and the large number of parameters to invert (72), the inverse problem we tried to solve is slightly under-determined, and only outer regions close to a strain gauges can be resolved with limited uncertainty. In the central part of the fault, where the maximum of slip occurs, uncertainty is of the order of 2 μm, which represents roughly 30% of the slip magnitude. This issue could probably be partly addressed by a denser strain gauge array, or by a different parametrization of fault slip, relying on the elliptical sub-fault approximation used for earthquake source characterization (Vallée & Bouchon, 2004; Di Carli et al., 2010; Twardzik et al., 2014). This would however be a strong assumption about the slow slip pattern, and the method should be adapted to the particularities of aseismic slip, as derived from geodetical studies in subduction zones for instance (Radiguet et al., 2011). We have also not tested yet whether Green's functions calculated assuming constant slip on one element instead of point delta sources would improve the inversion.

Furthermore, as revealed by the posterior joint PDF (Figures S21, S22 and S23), model parameters are to some extent correlated. The maximum slip Δu for instance is for some nodes positively correlated to the ramp duration T (Figure S21). This suggests that the relevant parameter is the ratio $\Delta u/T$, which is an order of magnitude of the slip rate. Similarly, the arrival time t_0 and T are slightly negatively correlated for some nodes (Figure S23), indicating that a too early slip could be partly compensated by a longer ramp duration. Future attempts to perform kinematic inversion of nucleation in the laboratory could consider these correlations to adapt the parametrization.

Previous experimental studies dedicated to the nucleation of stick-slip instabilities identified three successive stages of slip evolution (Ohnaka, 2000; Latour et al., 2013; McLaskey, 2019; Guérin-Marthe et al., 2019): a quasi static phase where the slipping patch expands at constant (or slightly increasing) speed, followed by an accelerating phase where rupture speed increases exponentially and finally the dynamic rupture once the rupture speed reaches a few km.s^{-1}. The size of the slipping patch at the transition to dynamic rupture is called the critical nucleation length. In our imaging of slip evolution in space and time, we do not observe this evolution in three phases, but only a quasi-static expansion characterized by a roughly constant rupture speed (Figure 16). At the end of this process, the dynamic rupture occurs quasi instantaneously, without any accelerating transition. We interpret this behavior as a consequence of a sample size being smaller than the critical nucleation length L_c. To estimate L_c, we assume that the granite is characterized by a shear modulus $\mu = 26$ GPa and a critical slip for friction evolution $d_c = 5\ \mu$m of the order of the grain size resulting from fault polishing, as suggested by (Ohnaka & Shen, 1999). Rate-and-state parameters $b-a$ range between 0.002 and 0.01 and b between 0.005 and 0.015 (Marone, 1998; Mitchell et al., 2013). Furthermore, the loading setup leads to normal stress σ_n ranging between 100 and 120 MPa. With this range of values, the lowest possible estimate of the critical nucleation length from (Rubin & Ampuero, 2005) is about $L_b = 1.33\mu d_c/b\sigma_n \simeq 9.5$ cm, which is slightly larger than the fault length (8 cm). In estimating L_c we excluded the expression derived by (Ampuero & Rubin, 2008) for the slip-law, since we do not observe a shrinking nucleation patch. The quasi-static nucleation we observe can not develop to the accelerating stage because it reaches the fault edges, and a stick slip controlled by the stiffness of the loading system immediately occurs. This behavior would correspond to the domain I (rigid block stick slip) defined in Figure 1 of (Mclaskey & Yamashita, 2017). We thus observe here a frustrated nucleation process, that could be forced by the increase of stress related to the triaxial loading (about 10 MPa and 5.6 MPa of shear and normal stress increase during the 20 s of the nucleation). This interpretation should however be confirmed by a proper measure of frictional parameters, and in particular d_c that can range between 1 and 100 μm for bare, dry granite surfaces (Dieterich, 1979; Marone & Cox, 1994; Beeler et al., 1994; Marone, 1998; Harbord et al., 2017).

Furthermore, the experiments performed under direct shear conditions report expansion speed of aseismic slip fronts during the quasi static stage of nucleation ranging between 1 mm.s^{-1} (Selvadurai et al., 2017) and roughly 10 m.s^{-1} (Latour et al., 2013; Mclaskey & Yamashita, 2017; McLaskey, 2019; Guérin-Marthe et al., 2019; Cebry et al., 2022), and slip rates of the order of 10 μm.s^{-1} to 10 mm.s^{-1}. In the triaxial experiment analyzed here, the aseismic slip front migrates at a few hundreds of m.day^{-1}, that is about a few mm.s^{-1}, and slip rate reaches 0.25 μm.s^{-1}, which is in the lower range of what has been observed in previous experiments. The ratio between slip rate and expansion speeds is close to 10^{-4}, which is also consistent with previous experimental studies. Overall, our results are close to what is observed by (Selvadurai et al., 2017), where the nucleation process is also stopped when the quasi-static aseismic slip front reaches the boundaries of the sample. In all other studies, the nucleation develops entirely up to the dynamic rupture. The rupture speed is thus likely influenced by boundary effects related to the small finite size of the sample.

The differences between the nucleation observed here and in other setups can also be related to the material used (PMMA, rock), the geometry (2D direct shear, 3D for triaxial setup), the range of normal stress, and the loading rate. Granite is stiffer than PMMA (larger elastic moduli). The loading rate imposed in the present experiment during inter sticks-slip phase is between 0.5 and 0.6 MPa.s^{-1} (Figure 1), which is slightly larger than in the experiments of (McLaskey, 2019; Cebry et al., 2022; Selvadurai et al., 2017) where loading rates remain in the range 0.01 to 0.1 MPa.s^{-1}, but similar to the 0.36 MPa.s^{-1} used by (Latour et al., 2013).(Guérin-Marthe et al., 2019) tested a larger range of loading rates between 0.01 and 6 MPa.s^{-1}. Overall, the main differences are probably the normal stress level that is significantly larger here (100 to 120 MPa) than the range considered by previous studies on nucleation (limited at 20 MPa for direct shear), and the relatively high loading rate of about 0.5 $MPa.s^{-1}$. Normal stress and loading rate have a strong influence on the nucleation process as evidenced by (Latour et al., 2013; Kaneko et al., 2016; Guérin-Marthe et al., 2019; Marty et al., 2023): it is shown in these studies that increasing the normal stress and loading rate tend to increase the rupture speed and slip rates during the quasi-static phase. We would therefore expect to observe larger rupture speed in our experiment, which is not the case, providing further support to the hypothesis of a strong boundary effect.

The range of propagation speed estimated here during the nucleation phase is also several orders of magnitude smaller than the rupture speeds characterizing the stick slip events themselves ($cm.s^{-1}$ to $km.s^{-1}$), as shown by Passelègue et al. (2020). The same experimental setup therefore generates a wide spectrum of fault slip events, from slow aseismic to dynamic ruptures. The kinematic inversion of fault slip presented here could be extended to image the dynamic rupture occurring during the stick-slip events. This would require to compute fully dynamic Green's functions instead of the static Green's function used here. Determining the coseismic slip of the stick-slip event would also allow to determine the stress field left on the fault by the dynamic rupture, and evaluate whether it controls the nucleation location of the next event, as observed here in the central left part of the fault.

The high normal stress prevailing on the fault, the absence of fluid over pressure and the limited roughness of the interface were motivations to neglect fault opening in the computation of Green's functions. This assumption will however have to be revised when considering experiments with significant dilation or compaction originating from fault roughness (Ohnaka & Shen, 1999; Goebel et al., 2017) or over-pressurized fluids (Proctor et al., 2020).

Finally, the aseismic slip front propagation speed obtained here can be compared to the aseismic slip front speeds observed on natural faults. Aseismic slip driving earthquake swarms or tremor bursts migrate at speeds between 100 $m.day^{-1}$ and 10 $km.day^{-1}$ (Lohman & McGuire, 2007; Obara, 2010; De Barros et al., 2020; Sirorattanakul et al., 2022). Slow slip events in subduction zones expand at speeds ranging from 100 $m.day^{-1}$ to 10 $km.day^{-1}$ (Radiguet et al., 2011; Fukuda, 2018). Aftershocks are sometimes observed to migrate away from the main rupture, at speeds of several km per decade, a feature that is generally interpreted as resulting from the propagation of a postseismic aseismic slip front (Wesson, 1987; Peng & Zhao, 2009; Perfettini et al., 2019; Fan et al., 2022). Joint coseismic and postseismic dynamic rupture inversion of the Napa earthquake also revealed shallow afterslip propagating at about 1.5 $km.day^{-1}$ (Premus et al., 2022). The speed observed in the experiment analyzed here is in the lower range of estimates for natural faults. However further investigation on the role of normal stress, loading rate would be necessary before upscaling the experimental results to natural faults. Previous studies have revealed how normal stress, fault roughness, and loading rate influence the critical nucleation length (Latour et al., 2013; Guérin-Marthe et al., 2019), the duration and amount of precursory aseismic slip (Guérin-Marthe et al., 2023). Our approach could be applied to other experiments performed under different stress conditions and loading rates to better characterize the mechanical control on aseismic slip development during nucleation. Furthermore, these experiments generate acoustic emissions (Marty et al., 2023) that could be located with respect to the aseismic nucleation zone inferred from our kinematic inversion, in order to better constrain the relationship between aseismic slip and seismic activity. Exploring these questions will be the purpose of our future studies.

8 Conclusion

We have presented a kinematic inversion method to image aseismic slip on a centimetric scale laboratory fault loaded within a tri-axial setup. The forward model involves the computation of quasi-static Green's functions using 3D finite elements analysis accounting for the cylindrical geometry of the rock sample, and the experimental loading conditions. After a series of synthetic tests allowing to better constrain the performance of the inversion method with respect to the configuration of the strain gauge array, we tested our method on a fault reactivation experiment. We showed that the nucleation of a stick-slip event consists of an aseismic slip event propagating as a quasi-static crack like pattern, at a speed of the order of 200 m.day^{-1} and leading to about 7 ± 2 μm of slip over a few tens of seconds before degenerating into a dynamic rupture. This first attempt to image the dynamics of fault slip in the laboratory demonstrates the potential of strain inversion to better characterize earthquake nucleation process.

9 Open Research

To ensure full reproducibility and ease-of-use of our framework, we provide the data used to perform the inversions at (Dublanchet et al., 2024).

Acknowledgments

The authors thank Frantisek Gallovic, Paul Selvadurai, two anonymous reviewers and the associate editor for their insightful comments that improved the manuscript. F.X.P acknowledges funding from the European Union (ERC Starting Grant HOPE num. 101041966).

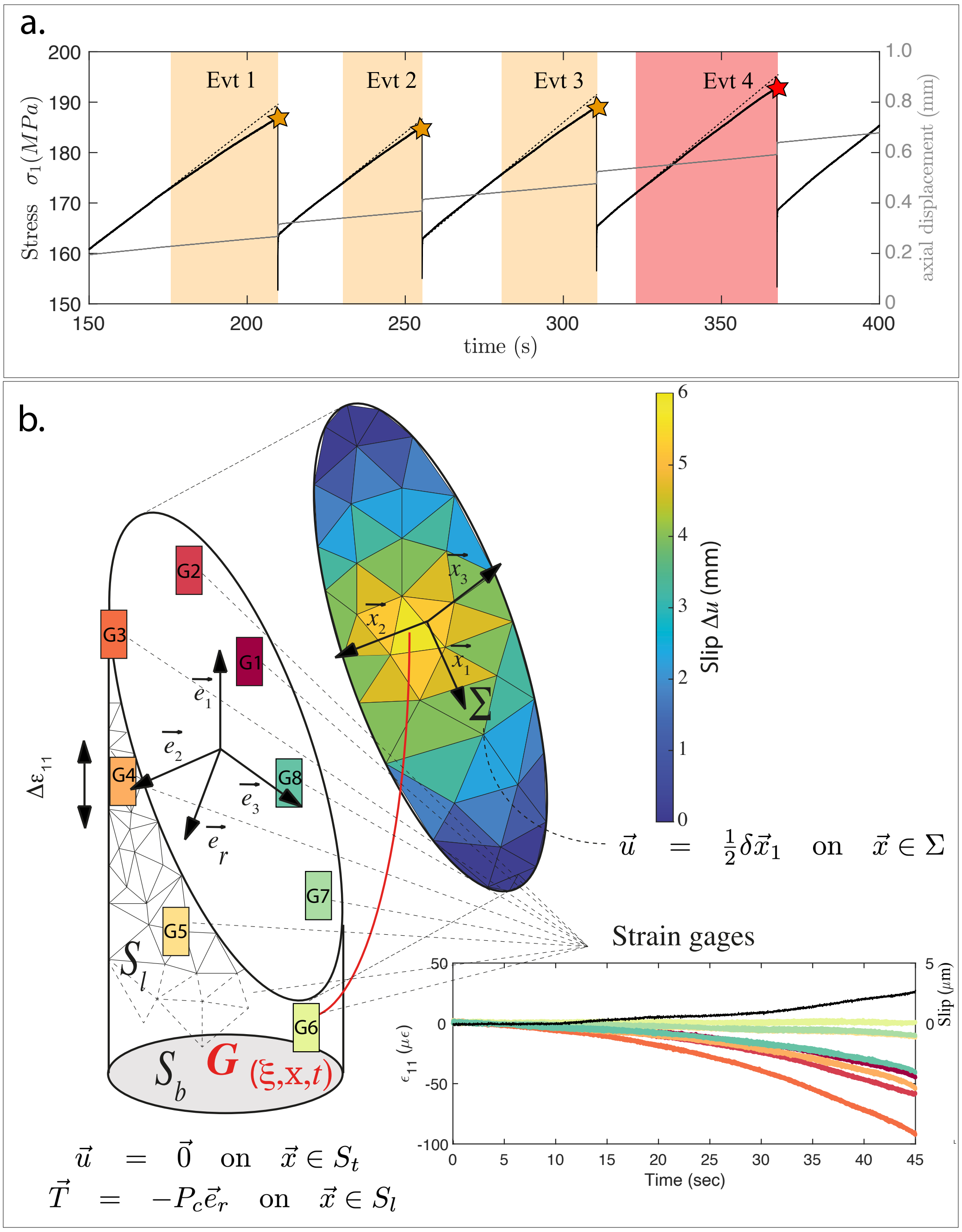

Figure 1. Experimental data set of stick-slip nucleation and description of the experimental setup and the forward problem a. Evolution of the axial stress σ_1 and of the external axial displacement during the loading along the fault interface. Orange and red time-windows correspond to the stages during which the fault exhibits inelastic slip, i.e. so-called preseismic or nucleation stage. The black dotted line indicates the elastic response. The red time-window corresponds to the experimental data used in the kinematic model presented in b. Red stars indicate dynamic events. b. Schematic view of the fault system geometry and of the boundary conditions applied in the finite element simulations. The inset presents the evolution of the inelastic axial strain ε_{11} prior to the stick-slip event (Evt4) (colorcode corresponds to the position of the strain gauges represented in the scheme of the sample assemblage. The black solid line in the inset corresponds to the fault slip prior instability.

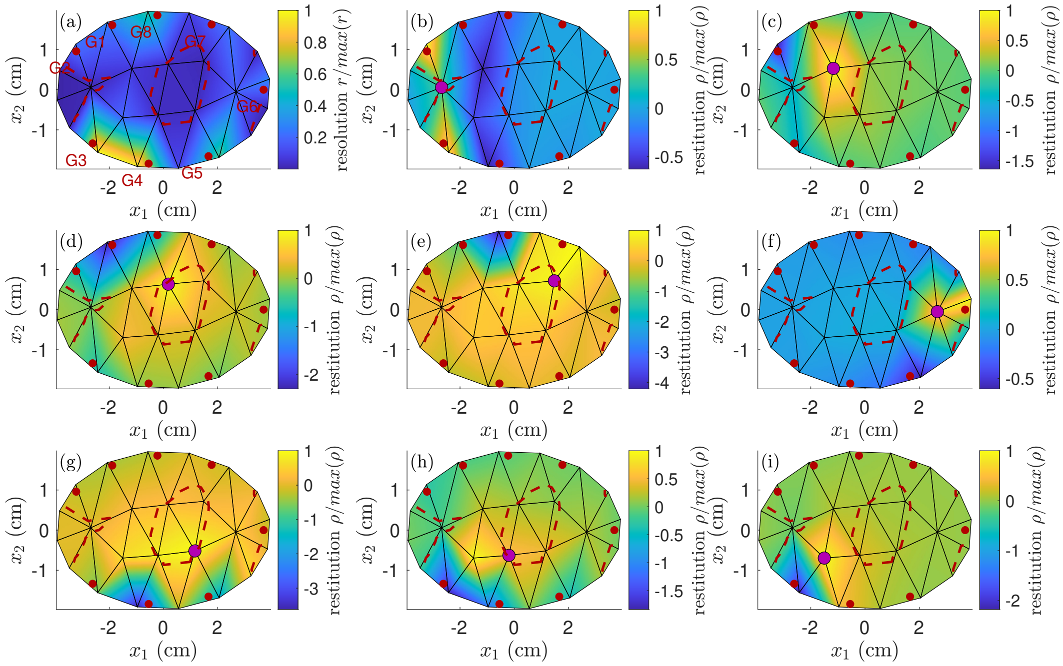

Figure 2. Resolution of the experimental array. (a) Diagonal elements r_i of the resolution matrix defined in equation (18), represented on the fault plane. The solid black lines indicate the mesh, and the red dots the experimental gauges array (strain gauges are labeled G1 to G8). The heavy red dashed line indicates a normalized resolution of 0.05. (b) to (j): Restitution ρ_i (off-diagonal elements of the resolution matrix) for the central nodes of the fault (magenta dots).

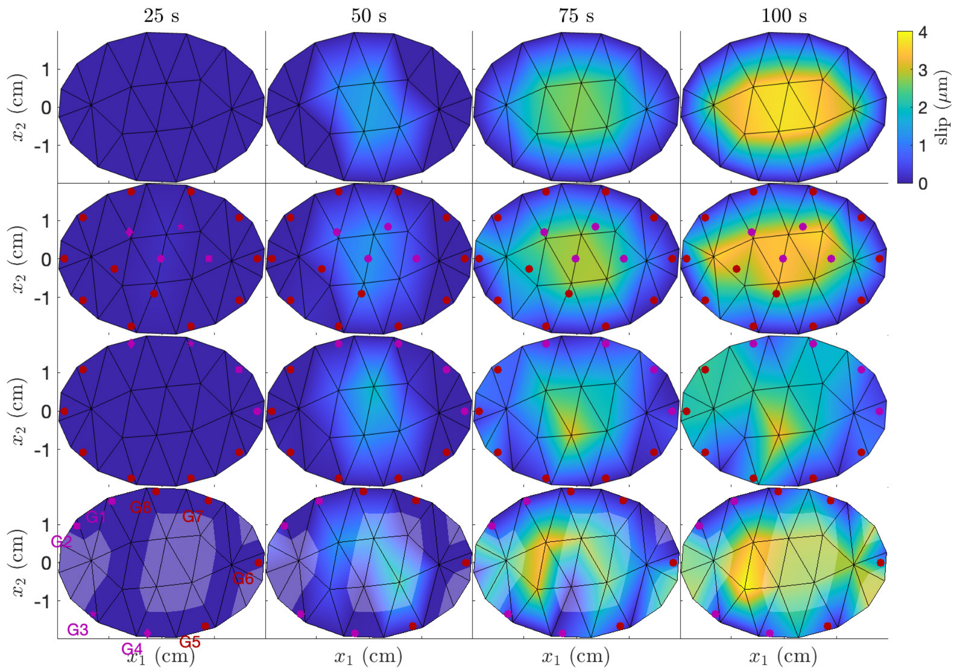

Figure 3. Synthetic test with elliptical crack growth: fault slip distribution. Each panel is a top view of the fault, showing the fault slip distribution δ (color-scale) at the time indicated in the title. The top row shows the true model to be retrieved, the others the inverted model with different strain gauges arrays. The triangular mesh used for the inversion is shown with solid black lines, and the projection of the strain gauges position is shown with red dots. The second row corresponds to the result of a deterministic inversion with the $N_g = 16$ gauges of SGA1, the second row with the $N_g = 10$ gauges of SGA2, and the last row with the $N_g = 8$ gauges (labeled G1 to G8) used in the real experimental setup (RSG, Figure 1a). The magenta symbols in all the panels indicate the position of gauges G1 (dot), G2 (square), G3 (star) and G4 (diamond) mentioned in Figure 5. The transparent cache on the panels of the last row indicates a resolution below 0.05 (see Figure 2 for details). The regularization parameter used here is $\lambda = 10^{-1}$.

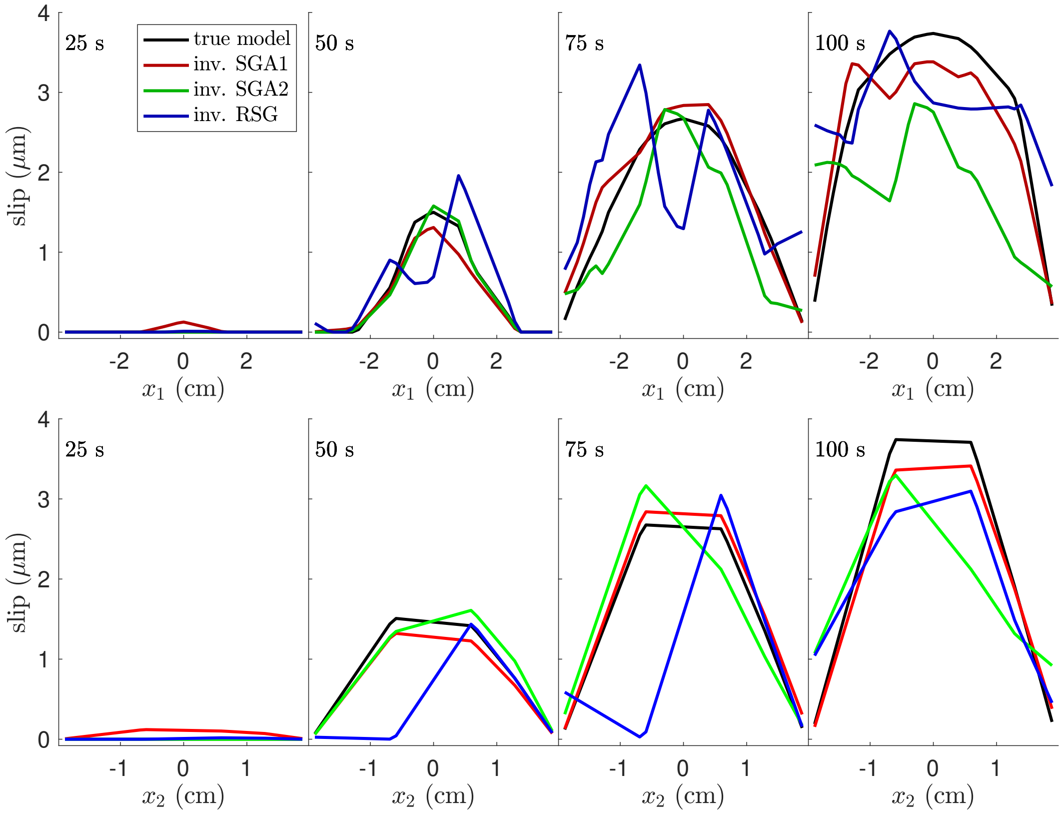

Figure 4. Synthetic test with elliptical crack growth: slip profiles. The top row shows slip profiles along x_1, the second row along x_2, obtained from Figure 3 at different times. The true model to be retrieved (from equation (19)) is shown in black, inverted model predictions in red (SGA1, $N_g = 16$), green (SGA2 $N_g = 10$) and blue (experimental setup RSG, $N_g = 8$).

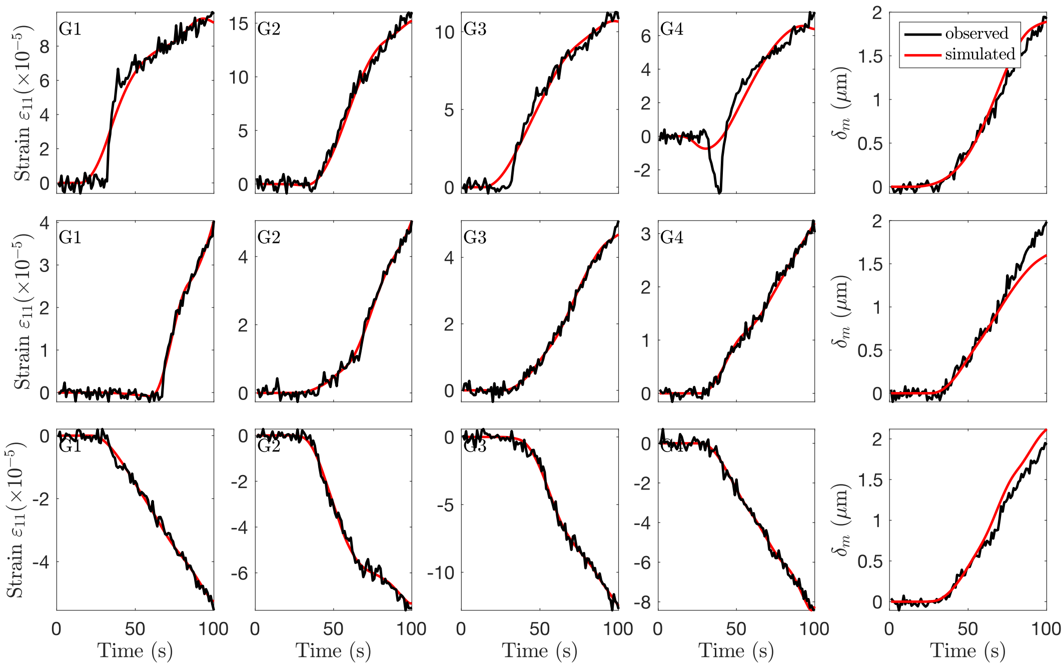

Figure 5. Synthetic test with elliptical crack growth: observed and simulated strain and slip. Each row corresponds to one synthetic test performed with one gauge array (first row: SGA1 $N_g = 16$, second row: SGA2 $N_g = 10$ and last row: experimental setup RSG, $N_g = 8$). Panels labeled G1, G2, G3 and G4 show the strain measured at the corresponding gauges (magenta symbols in Figure 3). The three right panels show the average slip δ_m. The black lines (observed) are the predictions of the true model, the red lines (simulated) are the predictions of the inverted models, shown in Figures 3 and 4.

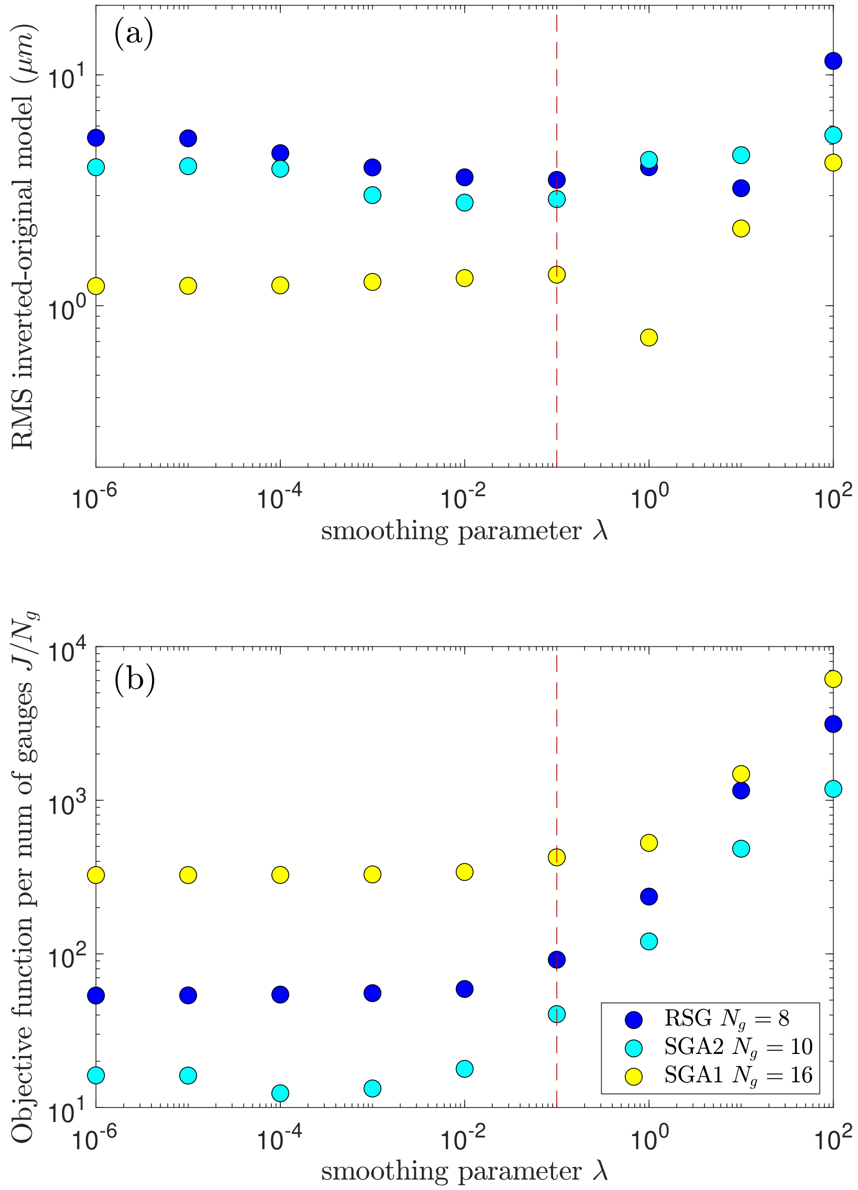

Figure 6. Synthetic tests summary. (a) RMS distance between true and inverted models. (b) Objective function per number of observations. The objective function is here the minimum value of J reached during the optimization, from equation (17). Colors refer to the strain gauge array. The red dashed vertical line indicates the optimal value of $\lambda = 10^{-1}$ used in the inversion of the real experimental data set.

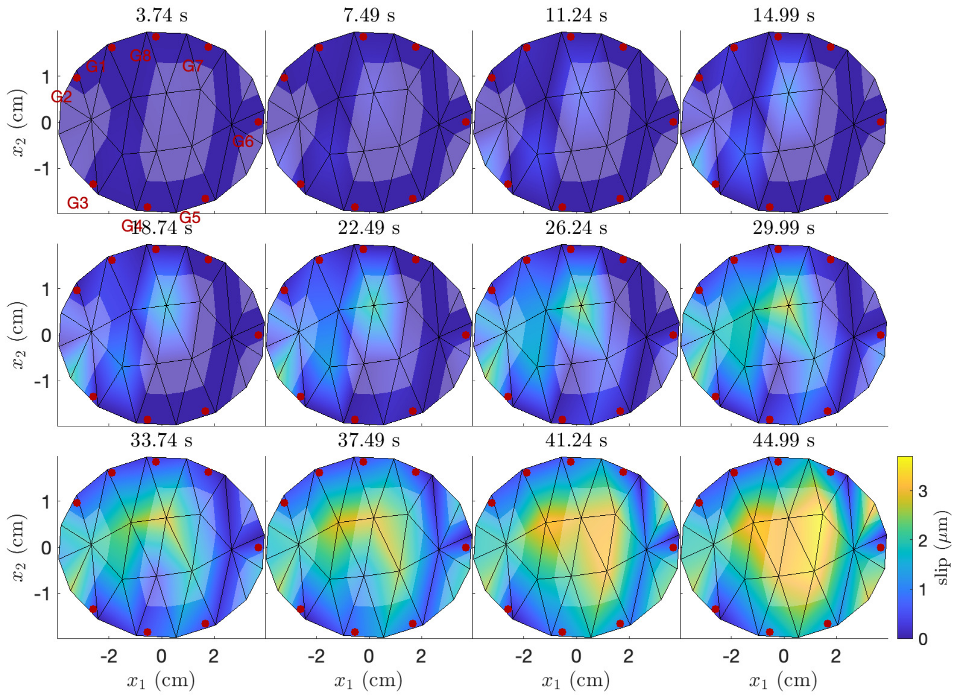

Figure 7. Kinematic inversion of Evt4 (nucleation phase), $\lambda = 10^{-1}$. Best model obtained from the deterministic inversion step. Each panel shows the inverted slip distribution at one time step indicated in the title. The mesh used for the inversion is shown as black solid lines and the experimental strain gauges (labeled G1 to G8) as red dots. The transparent cache indicates a resolution below 0.05, as defined in Figure 2a.

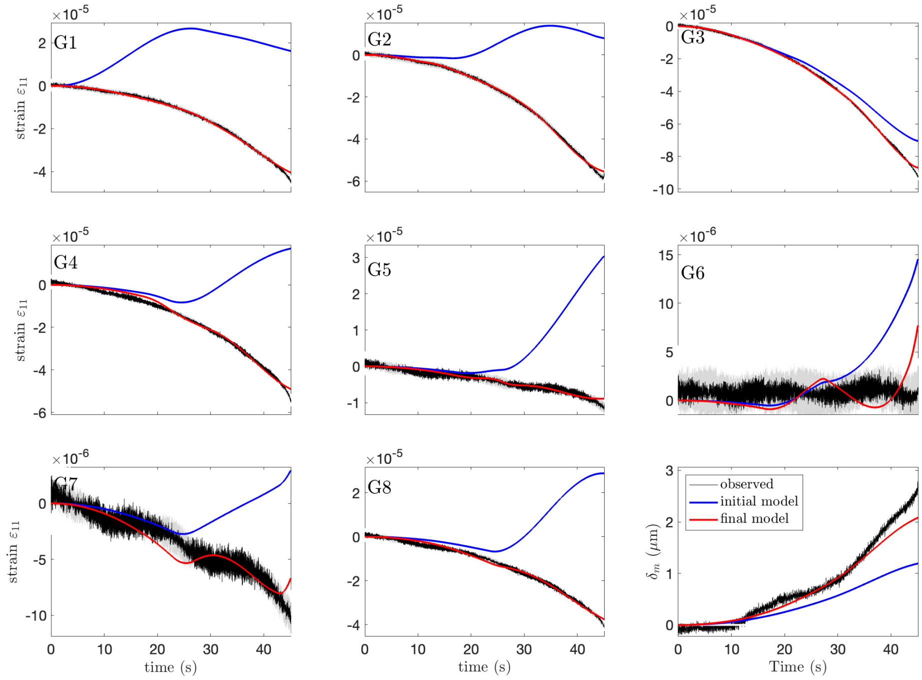

Figure 8. Observed (black) and modeled (red) strain and slip for the nucleation phase of Evt4. The model here is the outcome of the deterministic kinematic inversion of Evt4, shown in Figure 7. The strain gauges labels refer to Figure 7. The blue solid line indicates the prediction of the initial model used in the inversion. The gray shaded zone indicates the uncertainty on strain measurements used to construct the covariance matrices.

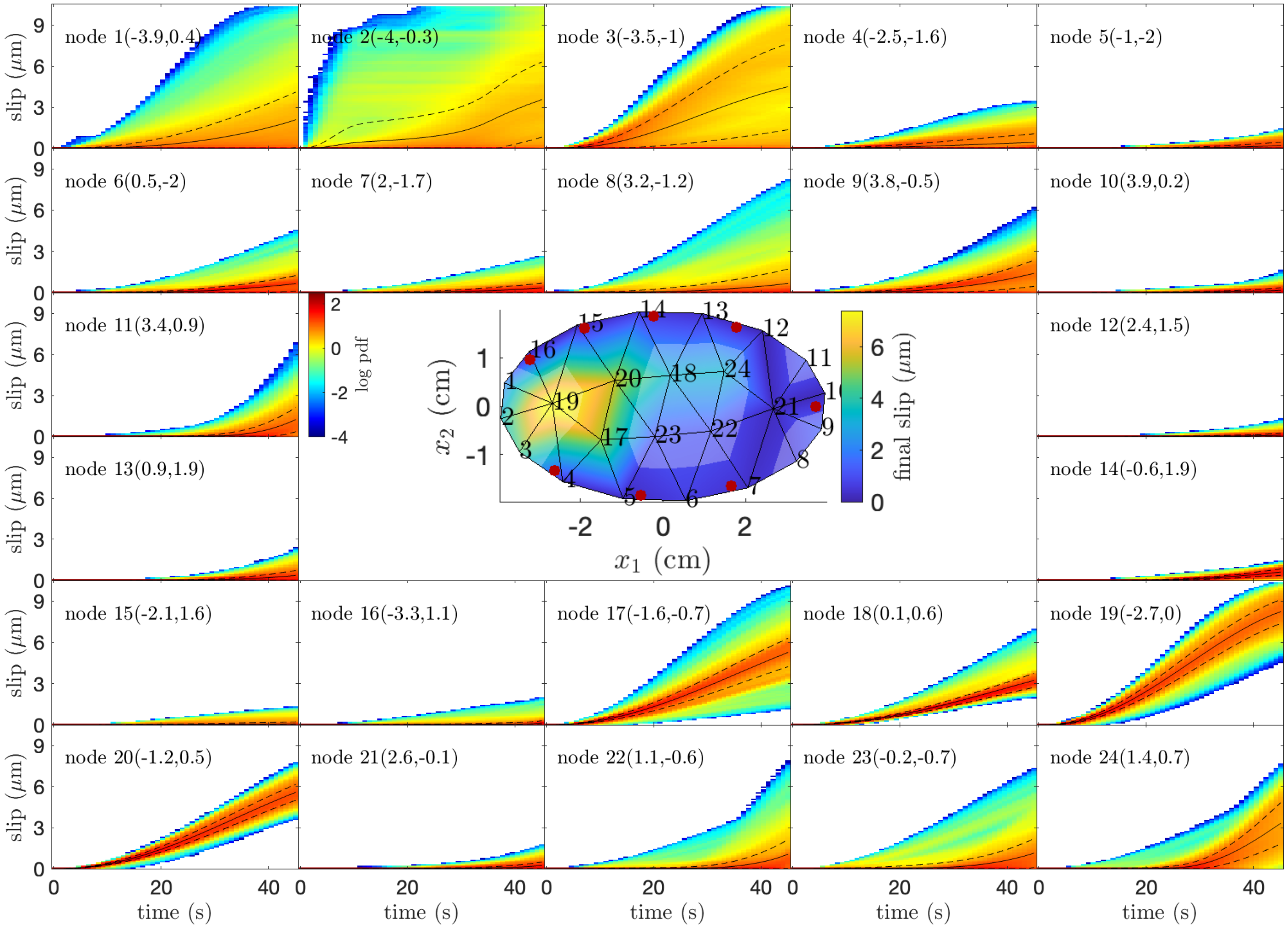

Figure 9. Kinematic inversion of Evt4: final slip distribution (mean model, middle map) and slip history at fault nodes (slip vs. time panels, one for each node). The colorscale of the panels refers to the posterior Probability Density Function (PDF) on slip, reconstructed from the MCMC exploration. The black solid line indicates the mean slip, as represented in Figure 10. The black dashed lines indicate the mean $\pm 1\sigma_\delta$. The node number and coordinates (in cm) are indicated in each panel. In the middle panel, strain gauges are shown as red dots, and the nodes numbering is also indicated in black.

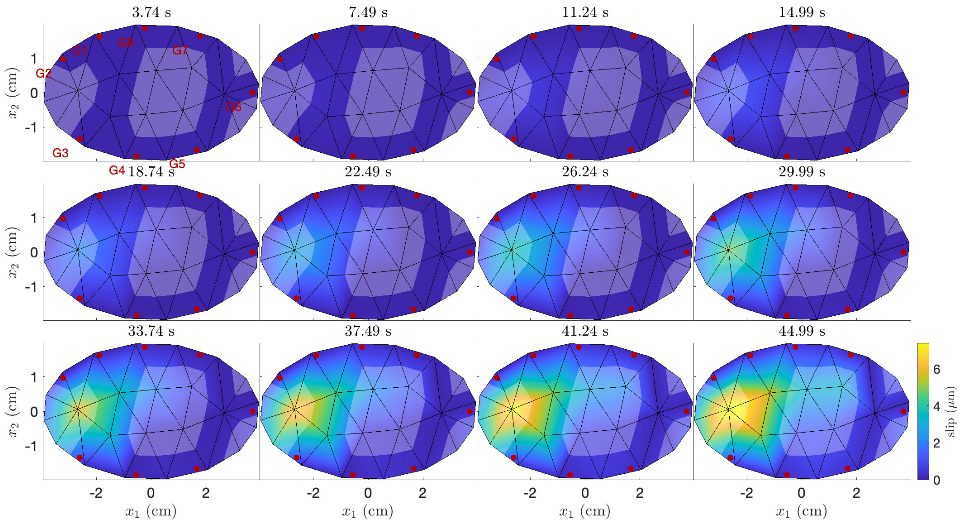

Figure 10. Kinematic inversion of Evt4 (nucleation phase). Mean model obtained from the Bayesian inversion step (MCMC). See Figure 7 for details about the representation.

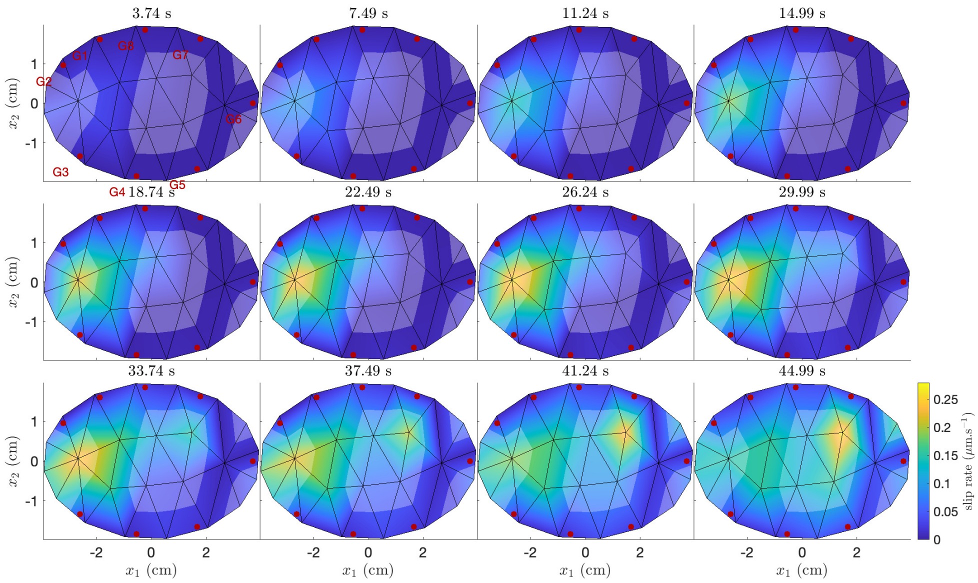

Figure 11. Kinematic inversion of Evt4 (nucleation phase). Slip rate derived from the mean MCMC model (Figure 10). See Figure 7 for details about the representation.

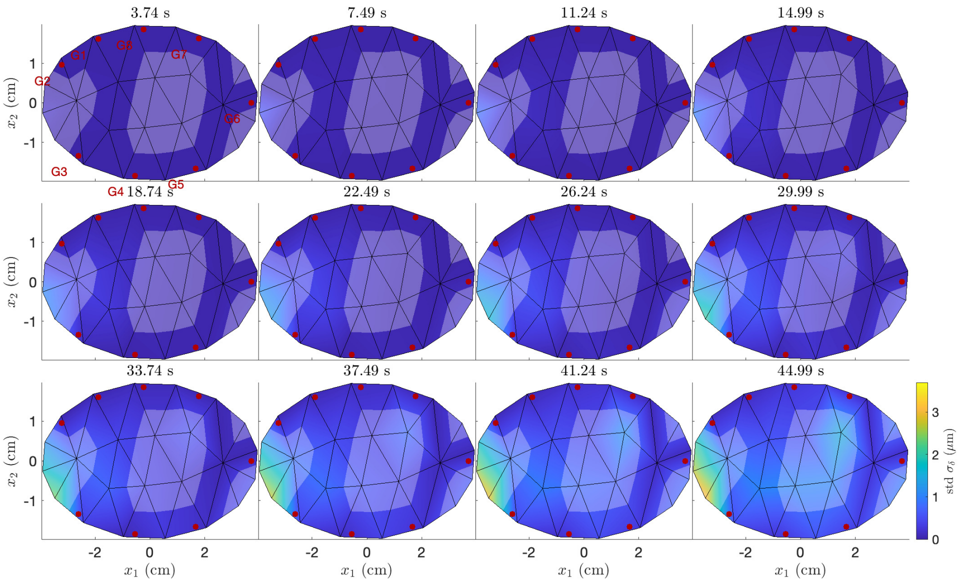

Figure 12. Kinematic inversion of Evt4: standard deviation on slip distribution σ_δ resulting from the Bayesian inversion step (MCMC). See Figure 10 for details about the representation.

References

Acosta, M., Passelègue, F. X., Schubnel, A., Madariaga, R., & Violay, M. (2019). Can precursory moment release scale with earthquake magnitude? a view from the laboratory. *Geophysical Research Letters*, *46*(22), 12927–12937.

Ampuero, J.-P., & Rubin, A. M. (2008). Earthquake nucleation on rate and state faults–aging and slip laws. *Journal of Geophysical Research: Solid Earth*, *113*(B1).

Anderlini, L., Serpelloni, E., & Belardinelli, M. E. (2016). Creep and locking of a low-angle normal fault: Insights from the altotiberina fault in the northern apennines (italy). *Geophysical Research Letters*, *43*(9), 4321–4329.

Avouac, J.-P. (2015). From geodetic imaging of seismic and aseismic fault slip to dynamic modeling of the seismic cycle. *Annual Review of Earth and Planetary Sciences*, *43*(1), 233-271. doi: 10.1146/annurev-earth-060614-105302

Beeler, N., Tullis, T., & Weeks, J. (1994). The roles of time and displacement in the evolution effect in rock friction. *Geophysical research letters*, *21*(18), 1987–1990.

Boudin, F., Bernard, P., Meneses, G., Vigny, C., Olcay, M., Tassara, C., . . . others (2022). Slow slip events precursory to the 2014 iquique earthquake, revisited with long-base tilt and gps records. *Geophysical Journal International*, *228*(3), 2092–2121.

Broyden, C. G. (1970). The convergence of a class of double-rank minimization algorithms: 2. the new algorithm. *IMA journal of applied mathematics*, *6*(3), 222–231.

Bürgmann, R. (2018). The geophysics, geology and mechanics of slow fault slip. *Earth and Planetary Science Letters*, *495*, 112–134.

Caballero, E., Duputel, Z., Twardzik, C., Rivera, L., Klein, E., Jiang, J., . . . others (2023). Revisiting the 2015 m w= 8.3 illapel earthquake: unveiling complex fault slip properties using bayesian inversion. *Geophysical Journal International*, *235*(3), 2828–2845.

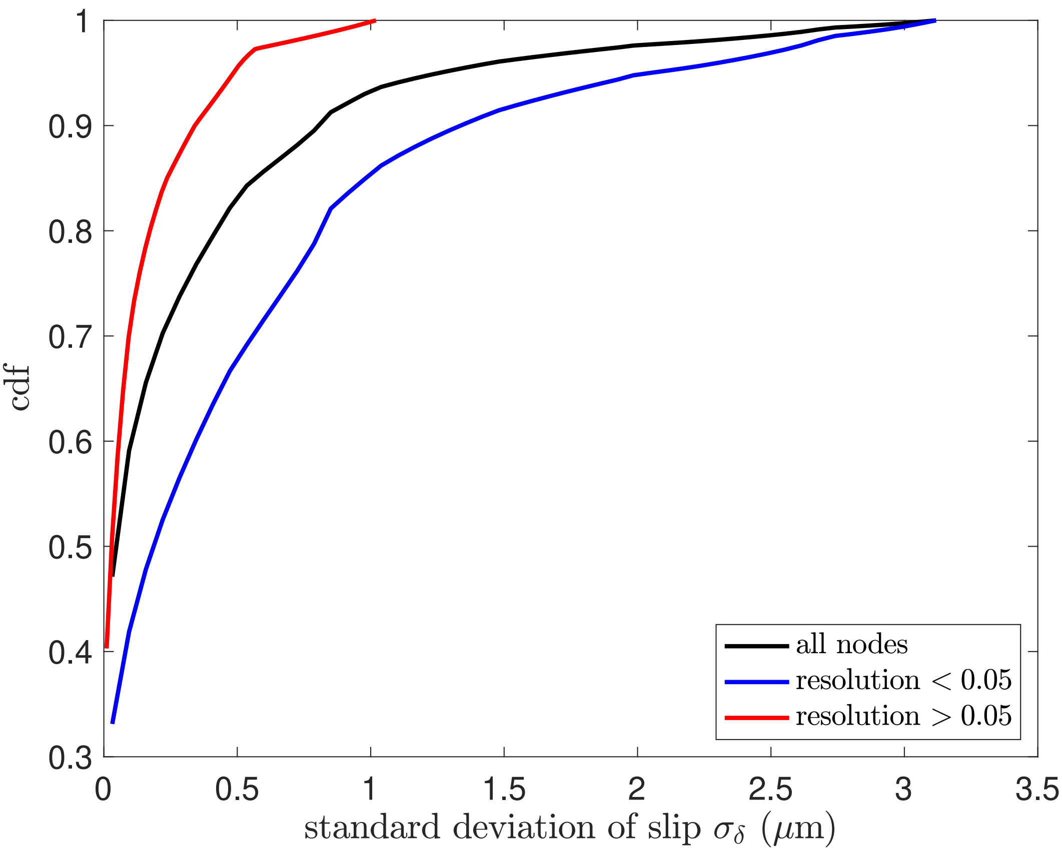

Figure 13. Distribution of standard deviation on inverted fault slip (cumulative density function cdf), derived from the Bayesian MCMC step for the kinematic inversion of Evt4 (nucleation phase). The black line corresponds to the all the σ_δ values obtained (all nodes, all time steps), The blue line corresponds to the nodes with resolution below 0.05 (all time steps), the red line with resolution larger than 0.05 (all time steps).

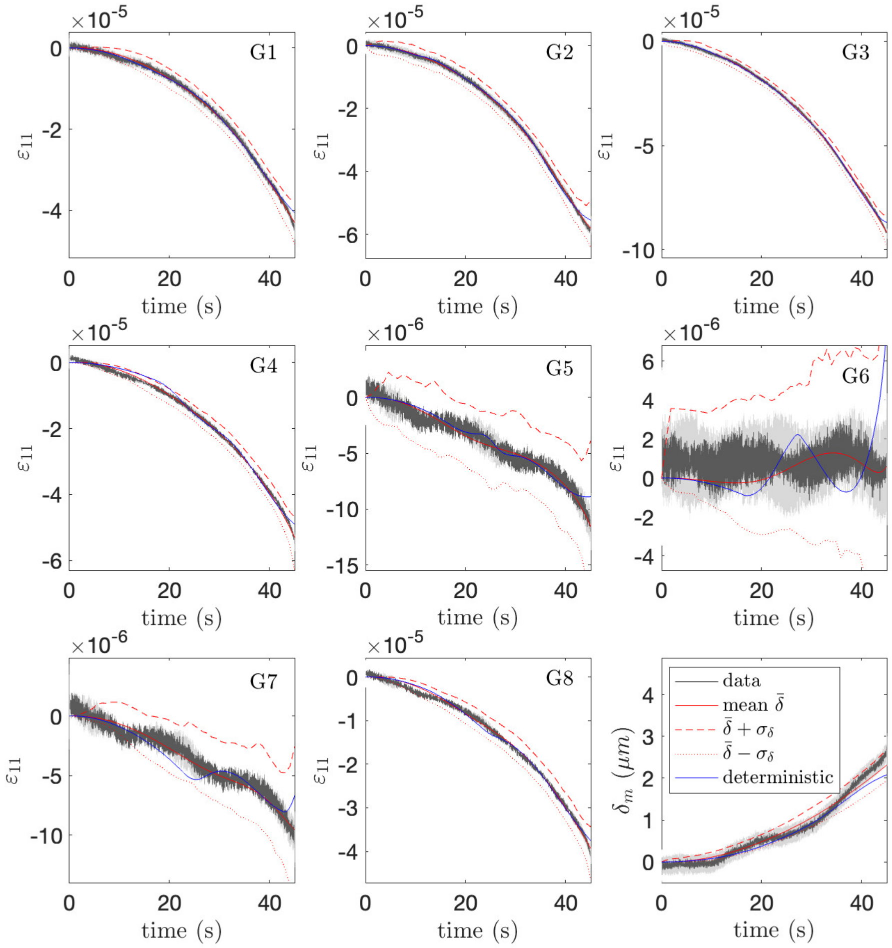

Figure 14. Observed (black) and modeled (red) strain and slip for Evt4. The models here are the outcome of the Bayesian MCMC step of the kinematic inversion of Evt4, (from Figures 10 and 12). The blue solid line indicates the prediction of the best model obtained in the deterministic step. The red solid line is the mean model prediction ($\bar{\delta}$), the dashed and dotted lines labeled $\bar{\delta} \pm \sigma_\delta$ indicate the strain range predicted by the models within one standard deviation, as defined in the main text. The gray shaded zone indicates the uncertainty on measurements, used to construct the covariance matrices.

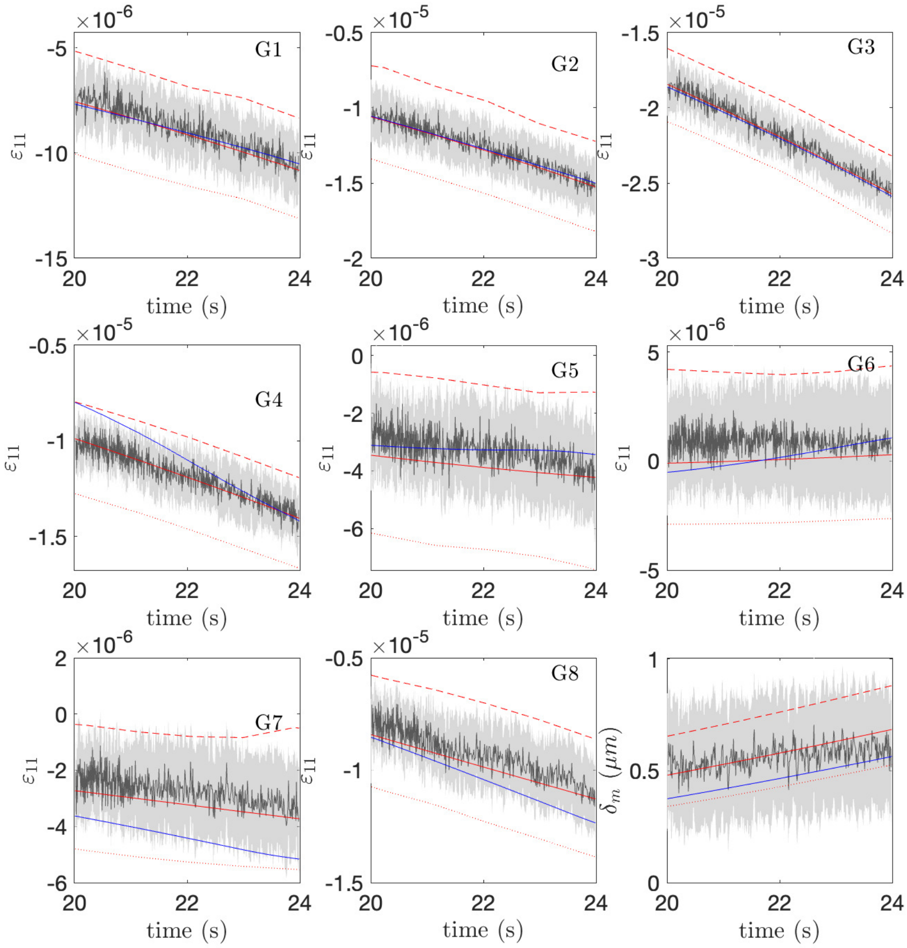

Figure 15. Detail of Figure 14, between 20 and 24 s.

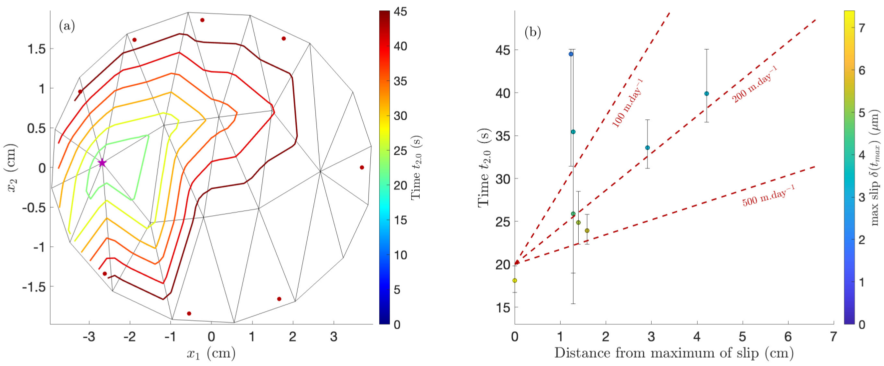

Figure 16. Time $t_{2.0}$ where slip exceeds 2 μm for Evt4, computed from the Bayesian step. (a): $t_{2.0}$ contours on the fault. The mesh is represented as black solid lines, red dots indicate the strain gauges. The star indicates the node experiencing the maximum slip on the fault; Coutours are plotted every 4.5 s. (b): $t_{2.0}$ vs. distance to the node experiencing maximum slip (star in Figure (a)). Only fault nodes experiencing more than 2 μm of slip in the mean MCMC model are represented here. The color indicates the inverted final slip $\delta(t_{max})$. Errorbars are derived from the σ_δ estimation. The red dashed lines indicate propagation speeds of 100, 200 and 500 m.day^{-1}.

Cebry, S. B. L., Ke, C.-Y., Shreedharan, S., Marone, C., Kammer, D. S., & McLaskey, G. C. (2022). Creep fronts and complexity in laboratory earthquake sequences illuminate delayed earthquake triggering. *Nature communications*, *13*(1), 6839.

De Barros, L., Cappa, F., Deschamps, A., & Dublanchet, P. (2020). Imbricated aseismic slip and fluid diffusion drive a seismic swarm in the corinth gulf, greece. *Geophysical Research Letters*, *47*(9), e2020GL087142.

Di Carli, S., François-Holden, C., Peyrat, S., & Madariaga, R. (2010). Dynamic inversion of the 2000 tottori earthquake based on elliptical subfault approximations. *Journal of Geophysical Research: Solid Earth*, *115*(B12).

Dieterich, J. H. (1979). Modeling of rock friction: 1. experimental results and constitutive equations. *Journal of Geophysical Research: Solid Earth*, *84*(B5), 2161–2168.

Dresen, G., Kwiatek, G., Goebel, T., & Ben-Zion, Y. (2020). Seismic and aseismic preparatory processes before large stick–slip failure. *Pure and Applied Geophysics*, *177*, 5741–5760.

Dublanchet, P., Passelègue, F. X., Chauris, H., Gesret, A., Twardzik, C., & Noël, C. (2024, January). *Strain and slip data for Kinematic inversion of fault slip during the nucleation of laboratory earthquakes [Dataset]*. Zenodo. Retrieved from `https://doi.org/10.5281/zenodo.10495680` doi: 10.5281/zenodo.10495680

Fan, L., Li, B., Liao, S., Jiang, C., & Fang, L. (2022). Precise earthquake sequence relocation of the january 8, 2022, qinghai menyuan ms6. 9 earthquake. *Earthq. Sci.*, *35*, 138–145.

Fletcher, R. (1970). A new approach to variable metric algorithms. *The computer journal*, *13*(3), 317–322.

Fletcher, R. (1982). A model algorithm for composite nondifferentiable optimization problems. *Nondifferential and Variational Techniques in Optimization*, 67–76.

Fukuda, J. (2018). Variability of the space-time evolution of slow slip events off the boso peninsula, central japan, from 1996 to 2014. *Journal of Geophysical Re-*

search: Solid Earth, *123*(1), 732–760.

Goebel, T. H., Kwiatek, G., Becker, T. W., Brodsky, E. E., & Dresen, G. (2017). What allows seismic events to grow big?: Insights from b-value and fault roughness analysis in laboratory stick-slip experiments. *Geology*, *45*(9), 815–818.

Goldfarb, D. (1970). A family of variable-metric methods derived by variational means. *Mathematics of computation*, *24*(109), 23–26.

Guérin-Marthe, S., Kwiatek, G., Wang, L., Bonnelye, A., Martínez-Garzón, P., & Dresen, G. (2023). Preparatory slip in laboratory faults: Effects of roughness and load point velocity. *Journal of Geophysical Research: Solid Earth*, *128*(4), e2022JB025511.

Guérin-Marthe, S., Nielsen, S., Bird, R., Giani, S., & Di Toro, G. (2019). Earthquake nucleation size: Evidence of loading rate dependence in laboratory faults. *Journal of Geophysical Research: Solid Earth*, *124*(1), 689–708.

Gvirtzman, S., & Fineberg, J. (2021). Nucleation fronts ignite the interface rupture that initiates frictional motion. *Nature Physics*, *17*(9), 1037–1042.

Gvirtzman, S., & Fineberg, J. (2023). The initiation of frictional motion—the nucleation dynamics of frictional ruptures. *Journal of Geophysical Research: Solid Earth*, *128*(2), e2022JB025483.

Harbord, C. W., Nielsen, S. B., De Paola, N., & Holdsworth, R. E. (2017). Earthquake nucleation on rough faults. *Geology*, *45*(10), 931–934.

Hartzell, S., Liu, P., Mendoza, C., Ji, C., & Larson, K. M. (2007). Stability and uncertainty of finite-fault slip inversions: Application to the 2004 parkfield, california, earthquake. *Bull. Seism. Soc. Am.*, *97*(6), 1911–1934. doi: 10.1785/0120070080

Hartzell, S. H., & Heaton, T. H. (1983). Inversion of strong ground motion and teleseismic waveform data for the fault rupture history of the 1979 imperial valley, california, earthquake. *Bulletin of the Seismological Society of America*, *73*(6A), 1553-1583. doi: 10.1785/BSSA07306A1553

Hastings, W. K. (1970). Monte carlo sampling methods using markov chains and their applications.

Hsu, Y.-J., Simons, M., Avouac, J.-P., Galetzka, J., Sieh, K., Chlieh, M., … Bock, Y. (2006). Frictional afterslip following the 2005 nias-simeulue earthquake, sumatra. *Science*, *312*(5782), 1921–1926.

Ide, S. (2007). *4.07 - slip inversion* (G. Schubert, Ed.). Amsterdam: Elsevier. doi: 10.1016/B978-044452748-6.00068-7

Inc., T. M. (2023). *Partial differential equation toolbox version: 3.10 (r2023a).* Natick, Massachusetts, United States: Author Retrieved from `https://www.mathworks.com`

Jolivet, R., Candela, T., Lasserre, C., Renard, F., Klinger, Y., & Doin, M.-P. (2015). The burst-like behavior of aseismic slip on a rough fault: The creeping section of the haiyuan fault, china. *Bulletin of the Seismological Society of America*, *105*(1), 480–488.

Kaneko, Y., Nielsen, S. B., & Carpenter, B. M. (2016). The onset of laboratory earthquakes explained by nucleating rupture on a rate-and-state fault. *Journal of Geophysical Research: Solid Earth*, *121*(8), 6071–6091.

Latour, S., Schubnel, A., Nielsen, S., Madariaga, R., & Vinciguerra, S. (2013). Characterization of nucleation during laboratory earthquakes. *Geophysical Research Letters*, *40*(19), 5064–5069.

Lawn, B. (1993). Fracture of brittle solids. *Cambridge solid state science series*, 307–334.

Liu, P., Custódio, S., & Archuleta, R. J. (2006). Kinematic inversion of the 2004 m 6.0 parkfield earthquake including an approximation to site effects. *Bulletin of the Seismological Society of America*, *96*(4B), S143–S158.

Lockner, D., Byerlee, J., Kuksenko, V., Ponomarev, A., & Sidorin, A. (1992). Observations of quasistatic fault growth from acoustic emissions. In *International geophysics* (Vol. 51, pp. 3–31). Elsevier.

Lohman, R., & McGuire, J. (2007). Earthquake swarms driven by aseismic creep in the salton trough, california. *Journal of Geophysical Research: Solid Earth*, *112*(B4).

Mai, P. M., Schorlemmer, D., Page, M., Ampuero, J., Asano, K., Causse, M., ... Zielke, O. (2016). The earthquake-source inversion validation (siv) project. *Seismological Research Letters*, *87*(3), 690-708. doi: 10.1785/0220150231

Marone, C. (1998). Laboratory-derived friction laws and their application to seismic faulting. *Annual Review of Earth and Planetary Sciences*, *26*(1), 643–696.

Marone, C., & Cox, S. (1994). Scaling of rock friction constitutive parameters: The effects of surface roughness and cumulative offset on friction of gabbro. *pure and applied geophysics*, *143*, 359–385.

Marty, S., Schubnel, A., Bhat, H., Aubry, J., Fukuyama, E., Latour, S., ... Madariaga, R. (2023). Nucleation of laboratory earthquakes: Quantitative analysis and scalings. *Journal of Geophysical Research: Solid Earth*, *128*(3), e2022JB026294.

McGuire, J. J., & Segall, P. (2003). Imaging of aseismic fault slip transients recorded by dense geodetic networks. *Geophysical Journal International*, *155*(3), 778–788.

McLaskey, G. C. (2019). Earthquake initiation from laboratory observations and implications for foreshocks. *Journal of Geophysical Research: Solid Earth*, *124*(12), 12882–12904.

McLaskey, G. C., & Kilgore, B. D. (2013). Foreshocks during the nucleation of stick-slip instability. *Journal of Geophysical Research: Solid Earth*, *118*(6), 2982–2997.

McLaskey, G. C., & Lockner, D. A. (2014). Preslip and cascade processes initiating laboratory stick slip. *Journal of Geophysical Research: Solid Earth*, *119*(8), 6323–6336.

Mclaskey, G. C., & Yamashita, F. (2017). Slow and fast ruptures on a laboratory fault controlled by loading characteristics. *Journal of Geophysical Research: Solid Earth*, *122*(5), 3719–3738.

Metropolis, N., Rosenbluth, A. W., Rosenbluth, M. N., Teller, A. H., & Teller, E. (1953). Equation of state calculations by fast computing machines. *The journal of chemical physics*, *21*(6), 1087–1092.

Michel, S., Gualandi, A., & Avouac, J.-P. (2019). Similar scaling laws for earthquakes and cascadia slow-slip events. *Nature*, *574*(7779), 522–526.

Mitchell, E., Fialko, Y., & Brown, K. (2013). Temperature dependence of frictional healing of westerly granite: experimental observations and numerical simulations. *Geochemistry, Geophysics, Geosystems*, *14*(3), 567–582.

Nielsen, S., Taddeucci, J., & Vinciguerra, S. (2010). Experimental observation of stick-slip instability fronts. *Geophysical Journal International*, *180*(2), 697–702.

Nishimura, T., Matsuzawa, T., & Obara, K. (2013). Detection of short-term slow slip events along the nankai trough, southwest japan, using gnss data. *Journal of Geophysical Research: Solid Earth*, *118*(6), 3112–3125.

Obara, K. (2010). Phenomenology of deep slow earthquake family in southwest japan: Spatiotemporal characteristics and segmentation. *Journal of Geophysical Research: Solid Earth*, *115*(B8).

Ohnaka, M. (2000). A physical scaling relation between the size of an earthquake and its nucleation zone size. *Pure and Applied Geophysics*, *157*(11), 2259–2282.

Ohnaka, M., & Shen, L.-f. (1999). Scaling of the shear rupture process from nucleation to dynamic propagation: Implications of geometric irregularity of the rupturing surfaces. *Journal of Geophysical Research: Solid Earth*, *104*(B1),

817–844.
Olson, A. H., & Apsel, R. J. (1982). Finite faults and inverse theory with applications to the 1979 imperial valley earthquake. *Bulletin of the Seismological Society of America*, *72*(6A), 1969-2001. doi: 10.1785/BSSA07206A1969
Ozawa, S., Nishimura, T., Munekane, H., Suito, H., Kobayashi, T., Tobita, M., & Imakiire, T. (2012). Preceding, coseismic, and postseismic slips of the 2011 tohoku earthquake, japan. *Journal of Geophysical Research: Solid Earth*, *117*(B7).
Passelègue, F. X., Almakari, M., Dublanchet, P., Barras, F., Fortin, J., & Violay, M. (2020). Initial effective stress controls the nature of earthquakes. *Nature communications*, *11*(1), 5132.
Passelègue, F. X., Aubry, J., Nicolas, A., Fondriest, M., Deldicque, D., Schubnel, A., & Di Toro, G. (2019). From fault creep to slow and fast earthquakes in carbonates. *Geology*, *47*(8), 744–748.
Passelègue, F. X., Latour, S., Schubnel, A., Nielsen, S., Bhat, H. S., & Madariaga, R. (2017). Influence of fault strength on precursory processes during laboratory earthquakes. *Fault zone dynamic processes: Evolution of fault properties during seismic rupture*, 229–242.
Passelègue, F. X., Schubnel, A., Nielsen, S., Bhat, H. S., Deldicque, D., & Madariaga, R. (2016). Dynamic rupture processes inferred from laboratory microearthquakes. *Journal of Geophysical Research: Solid Earth*, *121*(6), 4343–4365.
Peng, Z., & Zhao, P. (2009). Migration of early aftershocks following the 2004 parkfield earthquake. *Nature Geoscience*, *2*(12), 877–881.
Perfettini, H., Frank, W., Marsan, D., & Bouchon, M. (2019). Updip and along-strike aftershock migration model driven by afterslip: Application to the 2011 tohoku-oki aftershock sequence. *Journal of Geophysical Research: Solid Earth*, *124*(3), 2653–2669.
Premus, J., Gallovič, F., & Ampuero, J.-P. (2022). Bridging time scales of faulting: From coseismic to postseismic slip of the m w 6.0 2014 south napa, california earthquake. *Science advances*, *8*(38), eabq2536.
Proctor, B., Lockner, D. A., Kilgore, B. D., Mitchell, T. M., & Beeler, N. M. (2020). Direct evidence for fluid pressure, dilatancy, and compaction affecting slip in isolated faults. *Geophysical Research Letters*, *47*(16), e2019GL086767.
Radiguet, M., Cotton, F., Vergnolle, M., Campillo, M., Valette, B., Kostoglodov, V., & Cotte, N. (2011). Spatial and temporal evolution of a long term slow slip event: the 2006 guerrero slow slip event. *Geophysical Journal International*, *184*(2), 816–828.
Rast, M., Madonna, C., Selvadurai, P. A., Wenning, Q. C., & Ruh, J. B. (2024). Importance of water-clay interactions for fault slip in clay-rich rocks. *Journal of Geophysical Research: Solid Earth*, *129*(4), e2023JB028235.
Rubin, A. M., & Ampuero, J.-P. (2005). Earthquake nucleation on (aging) rate and state faults. *Journal of Geophysical Research: Solid Earth*, *110*(B11).
Schmidt, D., Bürgmann, R., Nadeau, R., & d'Alessio, M. (2005). Distribution of aseismic slip rate on the hayward fault inferred from seismic and geodetic data. *Journal of Geophysical Research: Solid Earth*, *110*(B8).
Selvadurai, P. A., Glaser, S. D., & Parker, J. M. (2017). On factors controlling precursor slip fronts in the laboratory and their relation to slow slip events in nature. *Geophysical Research Letters*, *44*(6), 2743–2754.
Shanno, D. F. (1970). Conditioning of quasi-newton methods for function minimization. *Mathematics of computation*, *24*(111), 647–656.
Sirorattanakul, K., Ross, Z. E., Khoshmanesh, M., Cochran, E. S., Acosta, M., & Avouac, J.-P. (2022). The 2020 westmorland, california earthquake swarm as aftershocks of a slow slip event sustained by fluid flow. *Journal of Geophysical Research: Solid Earth*, *127*(11), e2022JB024693.

Tarantola, A. (2005). *Inverse problem theory and methods for model parameter estimation.* SIAM.

Thomas, M. Y., Avouac, J.-P., Champenois, J., Lee, J.-C., & Kuo, L.-C. (2014). Spatiotemporal evolution of seismic and aseismic slip on the longitudinal valley fault, taiwan. *Journal of Geophysical Research: Solid Earth*, *119*(6), 5114–5139.

Twardzik, C., Das, S., & Madariaga, R. (2014). Inversion for the physical parameters that control the source dynamics of the 2004 parkfield earthquake. *Journal of Geophysical Research: Solid Earth*, *119*(9), 7010–7027.

Twardzik, C., Duputel, Z., Jolivet, R., Klein, E., & Rebischung, P. (2022). Bayesian inference on the initiation phase of the 2014 iquique, chile, earthquake. *Earth and Planetary Science Letters*, *600*, 117835.

Twardzik, C., Vergnolle, M., Sladen, A., & Tsang, L. L. (2021). Very early identification of a bimodal frictional behavior during the post-seismic phase of the 2015 m w 8.3 illapel, chile, earthquake. *Solid Earth*, *12*(11), 2523–2537.

Vallée, M., & Bouchon, M. (2004). Imaging coseismic rupture in far field by slip patches. *Geophysical Journal International*, *156*(3), 615–630.

Vallée, M., Xie, Y., Grandin, R., Villegas-Lanza, J. C., Nocquet, J.-M., Vaca, S., ... others (2023). Self-reactivated rupture during the 2019 mw= 8 northern peru intraslab earthquake. *Earth and Planetary Science Letters*, *601*, 117886.

Wallace, L. M., Webb, S. C., Ito, Y., Mochizuki, K., Hino, R., Henrys, S., ... Sheehan, A. F. (2016). Slow slip near the trench at the hikurangi subduction zone, new zealand. *Science*, *352*(6286), 701–704.

Wesson, R. L. (1987). Modeling aftershock migration and afterslip of the san juan bautista, california, earthquake of october 3, 1972. *Tectonophysics*, *144*(1-3), 215–229.

W. Goebel, T., Schorlemmer, D., Becker, T., Dresen, G., & Sammis, C. (2013). Acoustic emissions document stress changes over many seismic cycles in stick-slip experiments. *Geophysical Research Letters*, *40*(10), 2049–2054.